Author/s:
Chung, J;Tilūnaitė, A;Ladd, D;Hunt, H;Soeller, C;Crampin, EJ;Johnston, ST;Roderick, HL;Rajagopal, V

Title:
IP3R activity increases propensity of RyR-mediated sparks by elevating dyadic [Ca2+]

Date:
2023-01-01

Citation:
Chung, J., Tilūnaitė, A., Ladd, D., Hunt, H., Soeller, C., Crampin, E. J., Johnston, S. T., Roderick, H. L. & Rajagopal, V. (2023). IP3R activity increases propensity of RyR-mediated sparks by elevating dyadic [Ca2+]. Mathematical Biosciences, 355, https://doi.org/10.1016/j.mbs.2022.108923.

IP_3R activity increases propensity of RyR-mediated sparks by elevating dyadic $[Ca^{2+}]$

Joshua Chung[1,2+], Agnė Tilūnaitė[1,3,+], David Ladd[1,3,4], Hilary Hunt[3], Christian Soeller[5], Edmund J. Crampin[1,3,4], Stuart T. Johnston[3,4], H. Llewelyn Roderick[2,*], Vijay Rajagopal[1,6,*]

[1] Department of Biomedical Engineering, The University of Melbourne, Melbourne, VIC 3010, Australia

[2] Laboratory of Experimental Cardiology, Department of Cardiovascular Sciences, KU Leuven, Belgium

[3] School of Mathematics and Statistics, The University of Melbourne, Melbourne, VIC 3010, Australia

[4] ARC Centre of Excellence in Convergent Bio-Nano Science and Technology, School of Chemical and Biomedical Engineering, The University of Melbourne, Melbourne, VIC 3010, Australia

[5] Institute of Physiology, University of Bern, Bern, Switzerland

[6] Baker Department of Cardiometabolic Health, The University of Melbourne, Melbourne, VIC 3010, Australia

[+] Authors contributed equally.

[*] Correspondence: vijay.rajagopal@unimelb.edu.au, llewelyn.roderick@kuleuven.be

Abstract

Calcium (Ca^{2+}) plays a critical role in the excitation contraction coupling (ECC) process that mediates the contraction of cardiomyocytes during each heartbeat. While ryanodine receptors (RyRs) are the primary Ca^{2+} channels responsible for generating the cell-wide Ca^{2+} transients during ECC, Ca^{2+} release via inositol 1,4,5-trisphosphate (IP_3) receptors (IP_3Rs) are also reported in cardiomyocytes and to elicit ECC-modulating effects. Recent studies suggest that the localization of IP_3Rs at dyads grant their ability to modify the occurrence of Ca^{2+} sparks (elementary Ca^{2+} release events that constitute cell wide Ca^{2+} releases associated with ECC) which may underlie their modulatory influence on ECC. Here, we aim to uncover the mechanism by which dyad-localized IP_3Rs influence Ca^{2+} spark dynamics. To this end, we developed a mathematical model of the dyad that incorporates the behaviour of IP_3Rs, in addition to RyRs, to reveal the impact of their activity on local Ca^{2+} handling and consequent Ca^{2+} spark occurrence and its properties. Consistent with published experimental data, our model predicts that the propensity for Ca^{2+} spark formation increases in the presence of IP_3R activity. Our simulations support the hypothesis that IP_3Rs elevate Ca^{2+} in the dyad, sensitizing proximal RyRs toward activation and hence Ca^{2+} spark formation. The stochasticity of IP_3R gating is an important aspect of this mechanism. However, dyadic IP_3R activity lowers the Ca^{2+} available in the junctional sarcoplasmic reticulum (JSR) for release, thus resulting in Ca^{2+} sparks with similar durations but lower amplitudes.

Keywords

Ca^{2+} microdomains, Ca^{2+} sparks, calcium, cardiomyocyte, IP_3R, RyR

Abbreviations

Ca^{2+}, calcium; $[Ca^{2+}]$, Ca^{2+} concentration; ECC, excitation contraction coupling; AP, action potential; RyR, ryanodine receptor; IP_3, inositol 1,4,5-trisphosphate; IP_3R, IP_3 receptor; IP_3R1, type 1 IP_3R; IP_3R2, type 2 IP_3R; $[IP_3]$, IP_3 concentration; LTCC, L-type Ca^{2+} channel; SR, sarcoplasmic reticulum; JSR, junctional SR; NSR, network SR; CICR, Ca^{2+}-induced Ca^{2+} release; GPCR, G protein-coupled receptor;

ET-1, endothelin-1; IICR, IP_3-induced Ca^{2+} release; CaM, calmodulin; TnC, troponin C; CSQ, calsequestrin; SERCA, sarco-endoplasmic reticulum ATPase; 1D, 1-dimensional; FDHM, full duration at half maximum

1 Introduction

Underpinning the heart's pumping action is the concerted contraction and relaxation of individual cardiomyocytes, governed by the excitation-contraction coupling (ECC) process (1). In ventricular cardiomyocytes, ECC is initiated by the depolarisation of the sarcolemma by an action potential (AP), which, through inducing opening of voltage-gated L-type Ca^{2+} channels (LTCCs), permits calcium (Ca^{2+}) influx into 10 – 15 nm wide microdomains delimited by T-tubules and the junctional cisternae of the sarcoplasmic reticulum (SR) (**Figure 1**). The Ca^{2+} influx into these microdomains (henceforth dyads) induces a larger Ca^{2+} release from the SR via resident ryanodine receptors (RyRs). This Ca^{2+}-induced Ca^{2+} release (CICR) raises the local dyadic Ca^{2+} concentration ($[Ca^{2+}]$), giving rise to elementary Ca^{2+} release events that underlie ECC known as Ca^{2+} sparks (2,3). By virtue of the distribution of T-tubules at ≈ 1.8 µm intervals that form dyads throughout the cell volume, the synchronous evocation of Ca^{2+} sparks at dyads by an AP facilitates the transient rise in cell-wide cytosolic Ca^{2+} levels. This Ca^{2+} transient provides sufficient Ca^{2+} to bind to troponin C (TnC) in myofilaments enabling the cross-bridge cycle that contracts the cardiomyocyte (1).

Like RyRs, inositol 1,4,5-trisphosphate (IP_3) receptors (IP_3Rs) are Ca^{2+}-regulated Ca^{2+} channels that reside on the SR of cardiomyocytes (4). IP_3Rs also require IP_3 for activation (5). IP_3 is produced following phospholipase C activation and phosphatidylinositol 4,5-bisphosphate hydrolysis downstream of G protein-coupled receptors (GPCRs) as well as certain receptor growth factor receptors (6). Indeed, ventricular cardiomyocytes stimulated by G_q-associated GPCR agonists, such as endothelin-1 (ET-1), lead to IP_3-induced Ca^{2+} release (IICR) via IP_3Rs, which are shown to promote ECC-modulating effects such as arrhythmia and positive inotropy (7–12).

Despite lower expression levels (13) and Ca^{2+} conductance (5) relative to RyRs, IP_3Rs may elicit these ECC-modulating effects by their localization to functionally relevant Ca^{2+} signalling sites in the cell (14). A notable example is the colocalization of IP_3Rs and RyRs at dyads (8,15). It has been recently shown that stimulating the activity of IP_3Rs significantly increases the frequency of dyadic Ca^{2+} spark events (15). In this regard, IICR is hypothesised to elevate Ca^{2+} in the dyad, thereby priming and recruiting otherwise "silent" RyRs for future Ca^{2+} releases (8,11,14,15). The resulting increase in propensity for Ca^{2+} spark formation is then proposed to contribute to the ECC-modulating effects observed (11,16).

Here, we employed computational modelling to simulate the effects of IICR in the dyad. We developed a 1D spatial model of a dyad containing RyRs and type 2 IP_3Rs (IP_3R2). Using this model, we varied the number of IP_3Rs in the dyad and simulated its effect on the local Ca^{2+} dynamics as well as the properties of Ca^{2+} sparks generated. Our model predicts that IP_3R activity increases the baseline dyadic $[Ca^{2+}]$ at the expense of that in the junctional SR (JSR). This elevation of dyadic $[Ca^{2+}]$ then sensitizes RyRs in the vicinity toward activation, consequently increasing the propensity of Ca^{2+} spark formation. The decrease in JSR Ca^{2+} thus resulted in Ca^{2+} sparks with lower amplitudes but a similar duration.

2 Methods

2.1 Model Formulation

We model the spatiotemporal evolution of $[Ca^{2+}]$ as a system of partial differential equations (PDEs) at three interconnected compartments: cytosol, JSR, and network SR (NSR). The spatiotemporal

evolution of [Ca^{2+}] in these compartments is described by the variables $[Ca^{2+}]_c$, $[Ca^{2+}]_{JSR}$, and $[Ca^{2+}]_{NSR}$ respectively. These are shown in order in the equations below.

$$\frac{\partial[Ca^{2+}]_c}{\partial t} = \mathcal{D}_c \frac{\partial^2[Ca^{2+}]_c}{\partial x^2} + \sum_{i=1}^{4} J_{B_i} + J_{RyR} + J_{IP_3R} - J_{SERCA} + J_{Leak}$$
$$\frac{\partial[Ca^{2+}]_{JSR}}{\partial t} = \mathcal{D}_{JSR} \frac{\partial^2[Ca^{2+}]_{JSR}}{\partial x^2} + J_{B_5} - \left(J_{RyR} + J_{IP_3R}\right) + J_{Refill}$$
$$\frac{\partial[Ca^{2+}]_{NSR}}{\partial t} = \mathcal{D}_{NSR} \frac{\partial^2[Ca^{2+}]_{NSR}}{\partial x^2} + J_{SERCA} - J_{Refill} - J_{Leak}$$

where $\mathcal{D}_c$, $\mathcal{D}_{JSR}$, and $\mathcal{D}_{NSR}$ represent the diffusivity of Ca^{2+} in the cytosol, JSR, and NSR compartments, respectively. J_{RyR} and J_{IP_3R} correspond to the Ca^{2+} release fluxes by open RyRs and IP$_3$Rs respectively. J_{SERCA} corresponds to the Ca^{2+} uptake flux by sarco/endoplasmic reticulum Ca^{2+} ATPase (SERCA). J_{Refill} corresponds to the Ca^{2+} refill flux from the NSR into the JSR compartment. J_{B_i} corresponds to the flux of Ca^{2+} binding to mobile and immobile buffer species i.

The reaction diffusion of Ca^{2+} buffers are described by

$$\frac{\partial[CaB_i]}{\partial t} = \mathcal{D}_{B_i} \frac{\partial^2[CaB_i]}{\partial x^2} - J_{B_i}$$

where $[CaB]_i$ corresponds to the concentration of Ca^{2+}-bound buffer species i, with $i \in \{1,2,3,4,5\}$ representing buffers ATP, calmodulin (CaM), Fluo-4, troponin C (TnC), and calsequestrin (CSQ) respectively. $\mathcal{D}_{B_i}$ corresponds to the diffusivity of Ca^{2+}-bound buffer species i. Immobile buffers TnC and CSQ have $\mathcal{D}_{B_4} = \mathcal{D}_{B_5} = 0$.

2.2 Calcium Fluxes

The flux for each buffer species i is given by

$$J_{B_i} = k_{off}[CaB_i] - k_{on}[Ca^{2+}]\left(\left[B_i^{Tot}\right] - [CaB_i]\right)$$

where $\left[B_i^{Tot}\right]$ corresponds to the total concentration of buffer species i. k_{on} and k_{off} corresponds to the forward and backward reaction rates of buffer species i with Ca^{2+} respectively.

The refill flux from the NSR to the JSR compartment is given by

$$J_{refill} = g_{refill}\left([Ca^{2+}]_{NSR} - [Ca^{2+}]_{JSR}\right)$$

where g_{refill} is the refill flux rate. Its value is adjusted to achieve a realistic JSR refill time constant of ~130 ms (17–19) in simulations where the number of IP$_3$Rs in their element (see **Figure 1**) is 10 as we assume this to be the average number of IP$_3$Rs in a cluster.

The release fluxes from RyRs and IP$_3$Rs are given by

$$J_{RyR} = n_{RyR} g_{RyR}\left([Ca^{2+}]_{JSR} - [Ca^{2+}]_c\right)$$
$$J_{IP_3R} = n_{IP_3R} g_{IP_3R}\left([Ca^{2+}]_{JSR} - [Ca^{2+}]_c\right)$$

where n_{RyR} and n_{IP_3R} correspond to the number of open RyRs and IP$_3$Rs, respectively, whereas g_{RyR} and g_{IP_3R} correspond to the flux rate of RyR and IP$_3$R release, respectively. The value of g_{RyR} was adjusted to yield a characteristic Ca^{2+} spark profile in the simulation condition where only RyRs are present in the dyad. g_{IP_3R} is set to be 2.85 times lower than g_{RyR} as the Ca^{2+} conductance of IP$_3$Rs is estimated to be lower than that of RyRs by that factor (5).

Fluxes due to SERCA uptake activity were directly adapted from (20), which takes the form

$$J_{SERCA} = 2v_{cycle}A_p$$

where v_{cycle} is the cycling rate per SERCA molecule and A_p is the cytosolic concentration of SERCA homogenously spread throughout the bulk cytosolic region. The complete expression of each term is provided in Supplementary Materials.

An SR leak flux was also introduced to maintain the cytosolic Ca^{2+} background concentration at 0.1 µM. We use the same formulation as the SERCA model to balance J_{SERCA} such that $[Ca^{2+}]_c$ does not fall below 0.1 µM. Therefore, the SR leak flux is expressed as

$$J_{Leak} = J_{SERCA}([Ca^{2+}]_c = 0.1)$$

All parameter values are listed in Supplementary Materials.

2.3 Calcium Channels

RyR and IP_3R Ca^{2+} channels are stochastically simulated in the model. The gating of each RyR is directly adapted from the 2-state RyR model developed in (21); IP_3Rs are modelled after the 6-state Siekmann model (22) that incorporates non-steady state kinetics developed and used in (23,24). Mathematical expressions of the IP_3R model used in (23,24) were parameterised specifically to fit the steady state intermodal transition rates of type 1 IP_3Rs (IP_3R1). IP_3R1 have different channel activities for the same range of $[Ca^{2+}]$ compared to IP_3R2, the isoform most expressed in cardiomyocytes (5). To obtain an IP_3R model specific to IP_3R2, we modified the coefficients and exponents of the IP_3R model used in (23,24) to fit the steady state intermodal transition rates of IP_3R2 instead using data obtained from (22). This modification is essential as IP_3R2 has a higher open probability at lower ranges of $[Ca^{2+}]$ relative to the IP_3R1 model used in (23,24) (compare **Figure 7**C and **Figure 7**D in Supplementary Materials), thus allowing IP_3R2 to remain active for longer in the conditions of the dyad. Full details are provided in Supplementary Materials. In simulations involving IP_3R2, its gating behaviour was computed at a fixed IP_3 concentration ($[IP_3]$) of 0.15 µM, similar to that used in (23).

2.4 Model Geometry

The dyad and its surrounding cytoplasmic space are represented on a 1-dimensional (1D) simulation domain of 8 µm length. The 1D simulation domain reflects the portion of a typical experimental confocal line scan taken where a dyad is located. The buffering of Ca^{2+} by mobile buffers ATP, CaM, and the Ca^{2+} indicator dye, Fluo-4 occurs throughout this domain. The domain consists of 200 elements of size 0.04 µm, with the center nine elements (0.36 µm long) representing the dyadic region where RyRs and IP_3Rs are placed (**Figure 1)**. Elements outside the dyadic region represent the bulk cytosol where Ca^{2+} is subject to additional buffering by TnC and sequestration into the NSR compartment by SERCA. In all simulations, the number of RyRs in their specified element is fixed at 15, consistent with the average number of RyRs in a cluster as determined by super resolution microscopy techniques in healthy cardiomyocytes (25–27). Similar data on IP_3R clusters are not yet available. Therefore, the number of IP_3Rs in their specified element is varied between 0, 5, 10, and 20, corresponding to circumstances where there are no, low, intermediate, and high levels of IP_3R expression relative to the number of RyRs. The JSR compartment is designated the same location and number of elements as the dyadic region. Open RyRs and IP_3Rs thus result in a Ca^{2+} flux from the JSR into the dyadic region of the cytosol that is driven by the difference in $[Ca^{2+}]$ between these two compartments. Ca^{2+} in the JSR is subject to buffering by CSQ and refill from the NSR compartment. The non-junctional regions of the NSR compartment are homogenously distributed with SERCA that pumps Ca^{2+} from the bulk cytosol into the SR. SR leak fluxes are likewise present along non-junctional regions of the NSR compartment

and leaks Ca^{2+} into the bulk cytosolic region to maintain a baseline [Ca^{2+}] of 0.1 µM in the cytosol. The aforementioned intercompartmental fluxes connect the compartments elementwise as illustrated in **Figure 1**. A no-flux condition was imposed on all boundaries of the simulation domain.

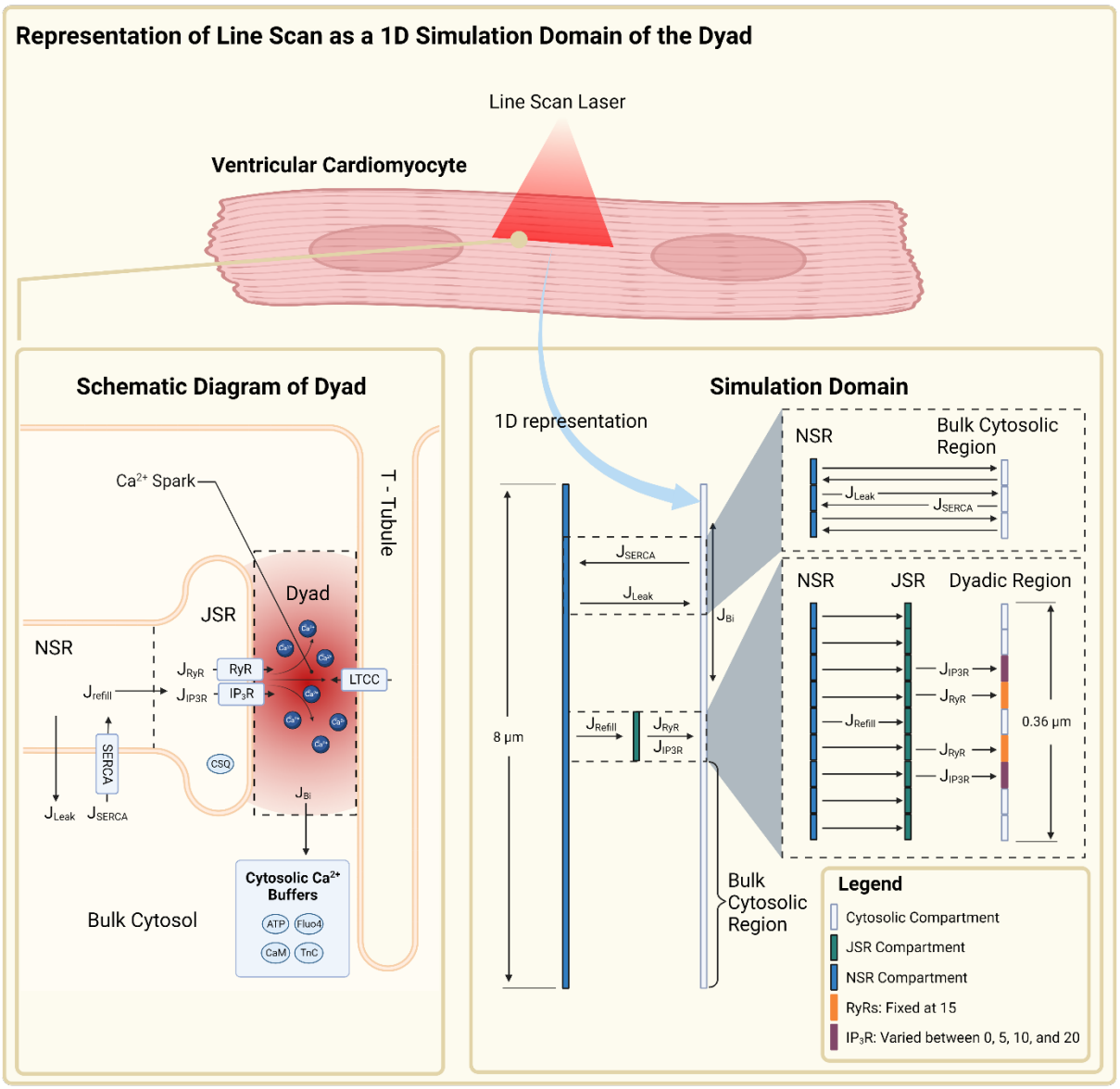

Figure 1. Schematic diagram of the compartments, fluxes, and arrangement of Ca^{2+}-handling proteins in the dyad and its 1D representation in the model. *The dyad is represented on an 8-µm, 1D computational domain with three compartments: cytosol, JSR, and NSR. The center nine elements of the cytosolic compartment represent the dyadic region where RyRs and IP_3Rs are located while the remaining elements represent the bulk cytosol where Ca^{2+} is additionally subject to J_{SERCA}, J_{Leak} and J_{B_4}. Ca^{2+} from the JSR is released into the dyadic region via open RyRs and IP_3Rs and diffuses along the cytosolic compartment, reacting with Ca^{2+} buffers before eventually being sequestered back into the NSR which refills the JSR.*

2.5 Calcium Spark Properties

We consider two properties of Ca^{2+} sparks in our results: amplitude and full duration at half maximum (FDHM). These two properties provide a measure of the magnitude and duration of the Ca^{2+} spark respectively. The amplitude of a Ca^{2+} spark is defined as the difference in [Ca^{2+}] from zero to the peak of the Ca^{2+} trace, whereas its FDHM is defined as the duration at which the Ca^{2+} spark exceeds half of its amplitude. The amplitude and FDHM of Ca^{2+} sparks are measured from their Ca^{2+} trace which is taken from the center of the dyad. An example of such a measurement is illustrated in **Figure 2**.

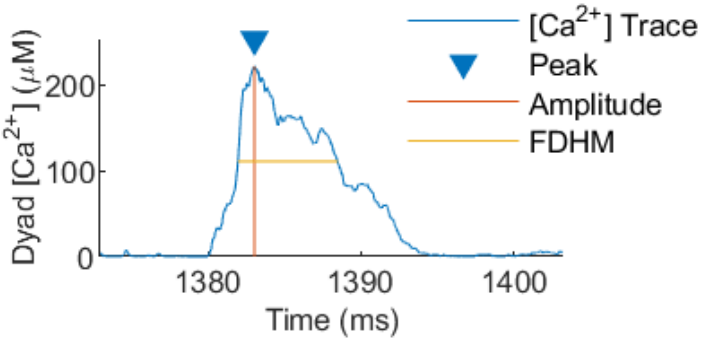

Figure 2. Plot showing the trace of a typical Ca^{2+} spark and measurements of its amplitude and FDHM. *The amplitude of a Ca^{2+} spark is measured as the difference between the peak of the Ca^{2+} trace (denoted by the inverted blue triangle) and the zero line. This is indicated by the vertical red line. The FDHM of a Ca^{2+} spark is measured as the duration at which the Ca^{2+} trace has a value that is greater than half of the amplitude. This is indicated by the horizontal yellow line.*

2.6 Numerical Methods and Implementation

The system of PDEs were discretised using the forward time centered space finite difference scheme, similar to (28). The resulting system of ODEs was solved using the explicit Euler method with adaptive time stepping capped at a maximum of 1×10^{-4} ms and a regular spatial resolution of 0.04 µm. Stochastic IP_3R and RyR gating states were solved using a hybrid Gillespie method as described in (29). The time at which any one receptor changes state may determine the time step forward for which the system is solved (adaptive time stepping). Simulations for each IP_3R number condition were repeated 200 times. In all simulations, the model was run for 1000 ms to ensure the system achieves steady state before they were analyzed to obtain the results presented. Recording of the simulations start at ≈ 950 ms, an earlier time point than the allocated 1000 ms for the system to achieve steady state. All codes and computations were implemented in MATLAB (The MathWorks Inc., Natick, Massachusetts).

3 Results

3.1 1D model reproduces calcium spark dynamics

The first column of **Figure 3**A illustrates the typical time evolution of $[Ca^{2+}]$ in different compartments of the model during a Ca^{2+} spark in RyR-only simulations i.e., no IP_3Rs. To replicate CICR during ECC that arise following the Ca^{2+} influx via LTCCs, Ca^{2+} sparks were initiated by introducing a 2-ms Ca^{2+} flux, reaching ≈ 30 µM, to elements in the dyadic region where RyRs are placed at the 1000 ms time point. This influx can be observed by the initial rise in $[Ca^{2+}]$ (with no variance) that is taken at the center element of the dyadic region. The resultant initial opening of RyRs occurs rapidly and releases a greater amount of Ca^{2+} from the JSR, thus providing a temporary positive feedback mechanism for the opening of other RyRs via CICR. RyRs open shortly after the initiating Ca^{2+} trigger and peaked at ≈ 13 RyRs for ≈ 9 ms before closing completely after ≈ 16 ms on average, consistent with simulation results from (21) whereby RyRs terminate after ≈ 20 ms of activity. During this time, dyadic $[Ca^{2+}]$ increased to ≈ 300 µM on average and declined back to ≈ 0.1 µM due to diffusion and chelation by buffers in the cytosol. Meanwhile, JSR $[Ca^{2+}]$ declines and reaches its nadir at ≈ 300 µM ≈ 13 ms after the initiation trigger, during which point RyRs have already begun closing. These results reinforce the induction decay mechanism of Ca^{2+} spark termination proposed by (30),whereby the decay of the Ca^{2+} flux through RyRs due to JSR depletion retards and eventually impedes inter-RyR regenerative CICR during a Ca^{2+} spark, thereby resulting in its termination. Following spark termination, JSR $[Ca^{2+}]$ is gradually replenished by that in the NSR at a time constant of ≈ 130 ms, consistent with experimental data (18,19). The JSR refill rate is adjusted to achieve this refill time constant in simulations where 10 IP_3Rs are present as we assume that to be the average number of IP_3Rs in a cluster. Together, our 1D model

of the dyad is capable of reproducing Ca^{2+} spark dynamics in reasonable agreement to that reported in other modelling and experimental studies (17–19,21).

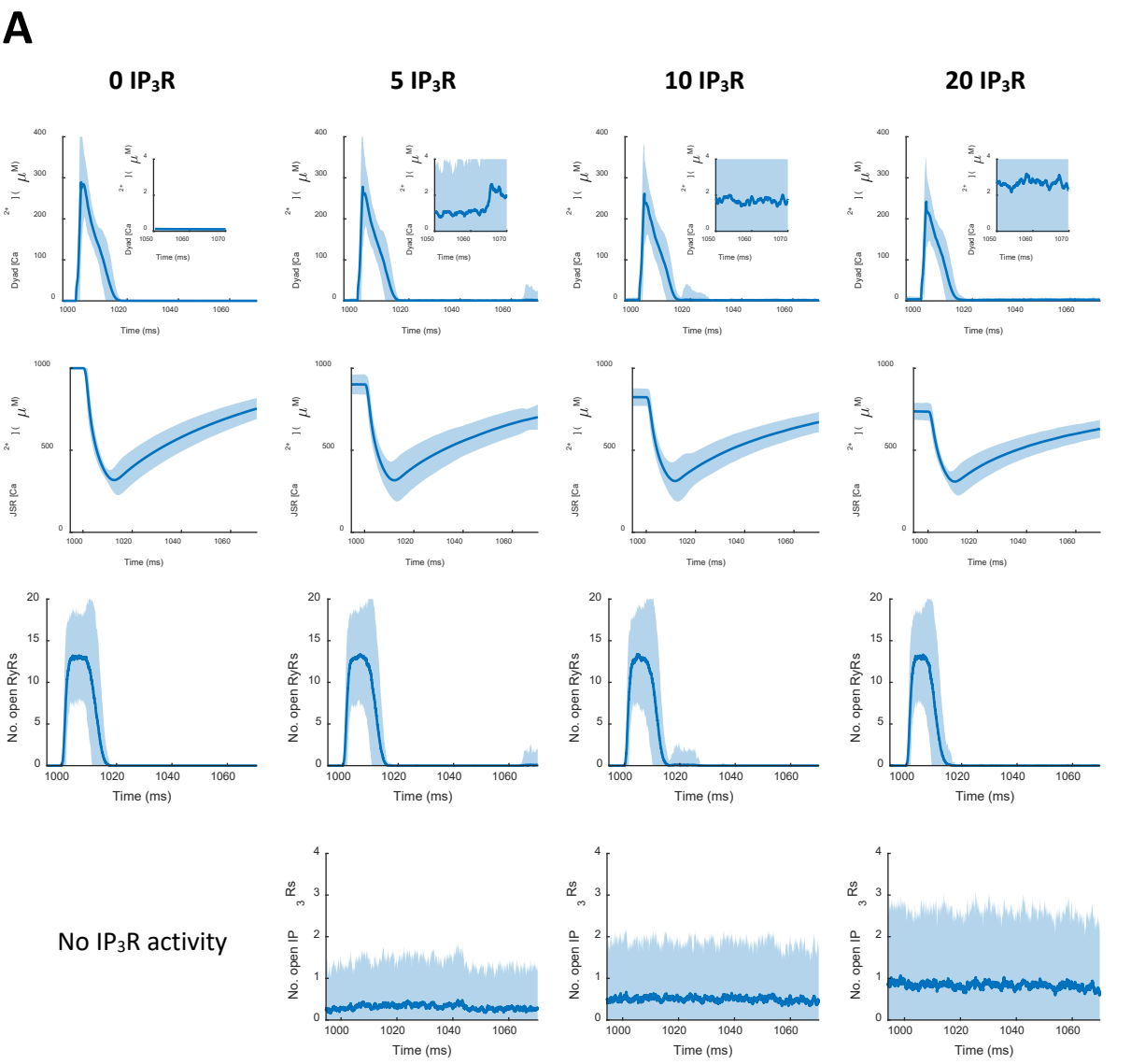

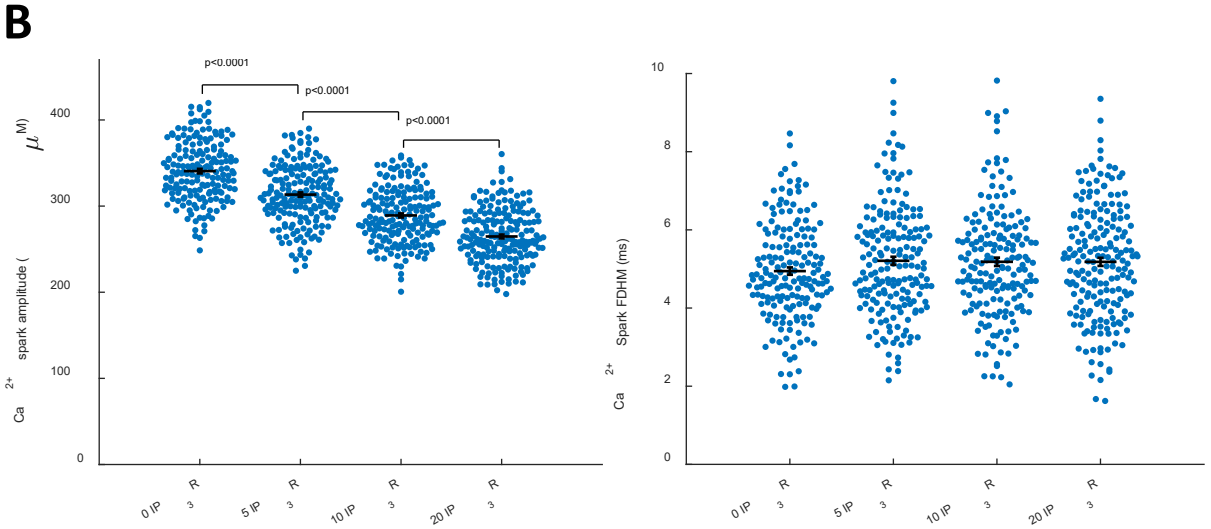

Figure 3. Ca^{2+} dynamics associated with LTCC-initiated Ca^{2+} sparks with different numbers of IP_3Rs in the dyad. A: *First to fourth row: Time evolution of dyadic [Ca^{2+}] (Notice the subtle progressive decrease in Ca^{2+} spark amplitude, reflected also in the leftmost swarm plot in* ***B****. Insets show an average baseline dyadic [Ca^{2+}] that increases with the number of IP_3Rs.), time evolution of JSR [Ca^{2+}], number of open RyRs, and number of open IP_3Rs associated with a Ca^{2+} spark. Mean and 95% confidence intervals, illustrated as solid lines and its surrounding shaded region respectively, are obtained from 200 simulations performed for each IP_3R number condition.* ***B:*** *Swarm plots showing a decreasing average Ca^{2+} spark amplitude but unchanged FDHM with increasing number of IP_3Rs. Analysis by 1 way ANOVA with Tukey-Kramer post hoc test. Data points are obtained from the same 200 simulations as that in* ***A****.*

3.2 Increased IP_3R2 expression decreases Ca^{2+} spark amplitude and Ca^{2+} stores

Figure 3A illustrates the effect of incorporating an increasing number of IP_3R2 in the dyad. Despite varying the number of IP_3Rs in the dyad, our model is capable of robustly simulating Ca^{2+} spark events. Due to the activity of IP_3Rs, their incorporation into the dyad essentially causes a Ca^{2+} "leak" from the JSR into the dyad. Hence, a 1000-ms wait time was allocated to allow the system to equilibrate to a steady state before simulating any Ca^{2+} release events. This amount of time was sufficient for the system to equilibrate as triggering Ca^{2+} sparks in simulations with longer wait times did not alter the resultant steady state [Ca^{2+}]. After equilibration, the average baseline dyadic [Ca^{2+}] rose above (insets of first row in **Figure 3**A) while that in the JSR fell below (second row of **Figure 3**A) the model's initial conditions of 0.1 µM and 1 mM respectively. Moreover, the magnitude of these changes increases with the number of IP_3Rs present in the dyad. We thus attribute these effects to the increased average number of open IP_3Rs (fourth row of **Figure 3**A). Altogether, our results suggest that the presence of IP_3R activity elevates dyadic [Ca^{2+}] at the expense of that in the JSR.

To test the effect of dyadic IP_3R activity on Ca^{2+} spark dynamics, we initiated Ca^{2+} sparks in simulations where IP_3Rs are present by similarly introducing a Ca^{2+} flux into RyR-containing elements as described earlier. Generated Ca^{2+} sparks have amplitudes that decrease with increasing number of IP_3Rs (**Figure 3**B). This correlates well with a lower JSR [Ca^{2+}] available for release at steady state. However, the duration of these Ca^{2+}-triggered Ca^{2+} sparks, measured by its FDHM, is not significantly different (**Figure 3**B). This result can also be indirectly inferred from the time to complete closing of RyRs and time to nadir of JSR [Ca^{2+}] that are not significantly altered with increasing number of IP_3Rs. Mechanistically, the elevated dyadic [Ca^{2+}] together with the lower JSR [Ca^{2+}] at steady state jointly results in RyR Ca^{2+} release fluxes that sustain inter-RyR CICR while depleting the JSR such that the Ca^{2+} spark duration remains unchanged. In all cases, the occurrence of Ca^{2+} sparks coincide with the transient opening of RyRs while the average IP_3R activity remained relatively constant throughout the simulation. This suggests that RyRs, and not IP_3Rs, are primarily responsible for the manifestation of Ca^{2+} sparks, which is consistent with experimental results that show an almost complete loss of Ca^{2+} sparks when RyRs are inhibited (15). Our model also successfully reproduced the experimental observation that JSR Ca^{2+} decreases to the same level after a Ca^{2+} spark event regardless of its initial concentration (19), further bolstering our confidence of this model in simulating Ca^{2+} sparks.

3.3 IP_3Rs increase propensity for spontaneous Ca^{2+} sparks in the dyad

By virtue of elevating dyadic [Ca^{2+}], IP_3Rs may play a role in enhancing the formation of Ca^{2+} sparks (8,14,15). Indeed, cardiomyocytes treated with G_q agonists or IP_3 exhibit an increased number of spontaneous Ca^{2+} spark events, which was attributed to IICR (7,8,31). But the mechanism underlying this observation is not fully resolved. To test whether the colocalization of IP_3Rs with RyRs in the dyad is responsible for the increase in spontaneous Ca^{2+} spark events, we performed simulations in the absence of LTCC initiations such that all Ca^{2+} sparks that are generated occur spontaneously. After a 1000 ms wait time for system equilibration, the model was allowed to run for a further 2000 ms from which our results were obtained. Simulations for each IP_3R number condition were repeated 200 times.

We recorded the number of Ca^{2+} spark events generated from these simulations and their associated properties (amplitude and FDHM). We find that the percentage of simulations with at least 1 Ca^{2+} spark event increases with the number of IP_3Rs (**Figure 4**A). Consistent with triggered Ca^{2+} sparks, the average amplitudes of spontaneously generated Ca^{2+} sparks decrease (**Figure 4**B) with increasing number of IP_3Rs while their FDHM remain unchanged (**Figure 4**C). We hypothesise that the increase in spontaneously generated Ca^{2+} sparks is due to the sensitization of RyRs by an elevated dyadic $[Ca^{2+}]$. To verify that RyRs are more active due to their sensitization by IICR, we also recorded the number of RyR openings that did not develop into full Ca^{2+} sparks (an example of detecting these events is shown in **Figure 8** of Supplementary Materials). Expectedly, the average number of RyR openings that do not lead to the formation of Ca^{2+} spark events also increased with the number of IP_3Rs in the dyad (**Figure 4**D), signifying that RyRs are indeed more active in the presence of more IP_3Rs. This increased number of spontaneous RyR openings raises the probability for Ca^{2+} spark formation and contributes to the decreased JSR $[Ca^{2+}]$ at steady state to some degree. Altogether, consistent with experimental data, our model predicts that the presence of dyadic IP_3R activity contributes to an increased occurrence of Ca^{2+} sparks and we attribute this increase in the number of spontaneous Ca^{2+} sparks to the increase in dyadic $[Ca^{2+}]$ brought about by IICR.

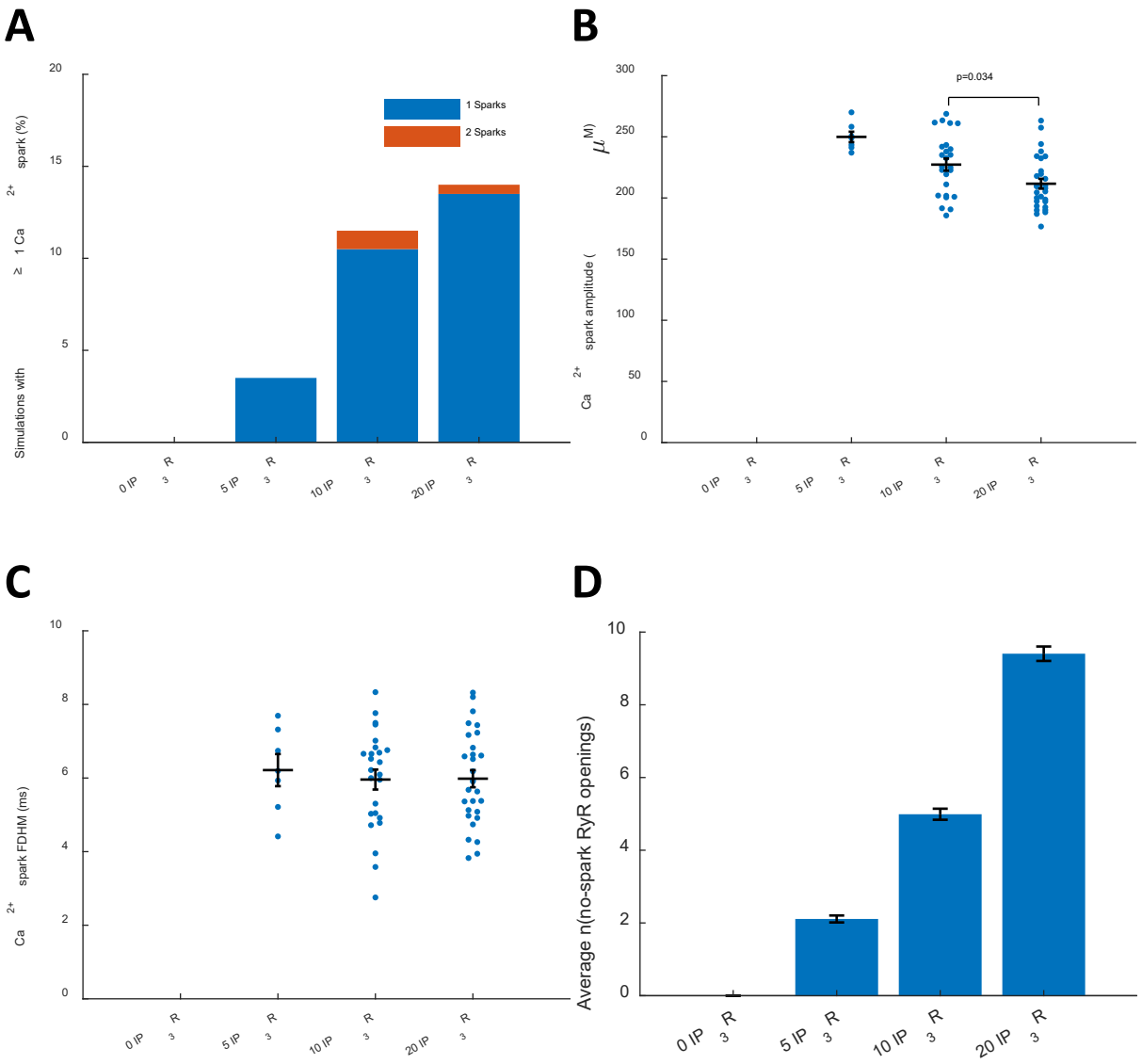

Figure 4. The number of spontaneous Ca^{2+} sparks increase with the number of IP_3Rs in the dyad. A: *Percentage of simulations where at least 1 Ca^{2+} spark event spontaneously occurred.* ***B:*** *Swarm plot showing the average amplitude of spontaneous Ca^{2+} spark events decrease with increasing number of IP_3Rs. Analysis by 1 way ANOVA with Tukey-Kramer post hoc test.* ***C:*** *Swarm plot showing the FDHM of spontaneous Ca^{2+} sparks that remains unchanged with the number of IP_3Rs. Analysis by 1 way ANOVA with Tukey-Kramer post hoc test.* ***D:*** *Average number of RyR opening events that do not lead to a Ca^{2+} spark increases with the number of IP_3Rs. All results presented in this figure are obtained from 200 simulations for each IP_3R number condition.*

3.4 Stochastic IP_3R gating behaviour is essential to effectively elicit spontaneous Ca^{2+} sparks

To explicitly correlate the increase in spontaneous Ca^{2+} sparks with dyadic [Ca^{2+}] elevation, we set out to artificially mimic the effect of IP_3R activity in the dyad. As indicated in our previous results (**Figure 3** and **Figure 4**), we expect that a simple elevation of dyadic [Ca^{2+}], consequent of an increased number of IP_3Rs, would increase the occurrence of spontaneous Ca^{2+} sparks. To this end, we first implemented a deterministic constant Ca^{2+} flux at IP_3R-containing elements in the dyadic region that continuously "leaks" Ca^{2+} from the JSR to artificially raise dyadic [Ca^{2+}]. The implementation of these Ca^{2+} fluxes is equivalent to specifying a number of IP_3Rs to be constitutively open throughout the time course of the simulation. To further illustrate the incremental effect of this constant dyadic [Ca^{2+}] elevation on spontaneous Ca^{2+} spark events, we specified the equivalent number of constitutively open IP_3Rs to manipulate the magnitude of the constant Ca^{2+} flux such that it qualitatively reflects the average Ca^{2+} dynamics result of our default model configuration for each IP_3R number condition (compare **Figure 3** and **Figure 10** in Supplementary Materials). 200 simulations were performed with this modification in the model. Surprisingly, the number of spontaneous Ca^{2+} spark events generated in this set of simulations were significantly lower than that in **Figure 4** and were insufficient for us to confirm our proposed mechanism (**Figure 11** in Supplementary Materials).

We hypothesized that this disparity arose due to the lack of randomness of the JSR Ca^{2+} "leak" fluxes which were originally provided by the stochastic gating of IP_3Rs. The randomness is associated with larger fluctuations of dyadic [Ca^{2+}] which should be more effective at opening RyRs due to its non-linear sensitivity to [Ca^{2+}] (see Section 7.2 of Supplementary Materials). To test this hypothesis, we implemented Ca^{2+} fluxes that randomly occur during the time course of the simulation for a randomly determined time interval in place of the constant deterministic Ca^{2+} fluxes previously described. Here, the incremental effect of an elevated dyadic [Ca^{2+}] was manipulated by adjusting the probability of an equivalent number of IP_3Rs to be open. This probability was likewise adjusted to yield qualitatively similar Ca^{2+} dynamics as that produced by our default model configuration for each IP_3R number condition (compare **Figure 3** and **Figure 13** in Supplementary Materials). 200 simulations were performed with this modification to the model, keeping all else constant. Remarkably, implementing a randomly occurring Ca^{2+} flux greatly increased the number of spontaneous Ca^{2+} spark events which displayed similar characteristics as those simulated by our default model configuration (compare **Figure 4** and **Figure 14** in Supplementary Materials). With these two sets of simulations, we not only correlated the increase in propensity of Ca^{2+} spark formation with dyadic [Ca^{2+}] elevation, but also demonstrated the significance of the stochastic nature of IP_3R gating that sporadically elevate dyadic [Ca^{2+}] to effectively elicit this outcome.

4 Discussion

While activating IP_3Rs in the cardiomyocyte influences Ca^{2+} handling and ECC (7–12), the mechanistic basis of this observation is not established. Recent evidence suggest that IICR modulates ECC through the localization of IP_3Rs to functionally important Ca^{2+} signalling sites (14), a quintessential example of which are dyads (8,15). Specifically, Ca^{2+} release via IP_3Rs expressed in the dyad is hypothesized to sensitize native RyRs, with which they colocalize, towards activation via IICR (8,14,15). Consequently,

the propensity for RyR opening and the formation of Ca^{2+} sparks (elementary Ca^{2+} release events underlying ECC-associated Ca^{2+} transients) is increased. Using a 1D model of the dyad that incorporate the behaviour of both RyRs and IP_3Rs, we set out to test this hypothesis while uncovering its underlying Ca^{2+} dynamics.

4.1 IP_3R-mediated Ca^{2+} release prime RyRs for release

A notable finding of our simulations is that the probability of spontaneous Ca^{2+} spark events increase with the number of IP_3Rs. We were also able to uncover the mechanism by which this occurs through our recording of $[Ca^{2+}]$ evolution with time at different compartments of the dyad. Our model predicts that while RyRs are almost always in their closed state at baseline $[Ca^{2+}]$ (third row of **Figure 3**A and **Figure 8**C), IP_3Rs exhibit greater activity, as evidenced by the number of open IP_3Rs throughout the simulation time course (fourth row of **Figure 3**A). This difference in behaviour is also correspondingly reflected in their open probability versus cytosolic $[Ca^{2+}]$ curves (32,33). Consequently, the activity of IP_3Rs in the dyad is akin to introducing a Ca^{2+} leak from the JSR into the dyad. Increasing the number of IP_3Rs increases the magnitude of this "leak", as can be seen from a lower average JSR $[Ca^{2+}]$ (second row of **Figure 3**A), due to an increased number of open IP_3Rs on average (fourth row of **Figure 3**A). This "eventless" and SR Ca^{2+}-modulating "leak" due to IICR is consistent with that proposed in (34). The consequent decrease in JSR $[Ca^{2+}]$ led to Ca^{2+} sparks with lower amplitudes. On the other hand, the average baseline dyadic $[Ca^{2+}]$ is increased due to this IICR (insets in first row of **Figure 3**A). This elevation in dyadic $[Ca^{2+}]$ sensitizes RyRs (as seen from an increased RyR activity in **Figure 4**C) thereby increasing the propensity for Ca^{2+} spark formation (**Figure 4**A).

In our efforts to fully elucidate the aforementioned mechanism, we find that an intermittent Ca^{2+} "leak" from the JSR into the dyad, granted by the stochasticity of IP_3R gating, is an essential feature to eliciting the spontaneous Ca^{2+} sparks observed. Our model predicts that an artificial sustained JSR $[Ca^{2+}]$ "leak", resulting in a constant dyadic $[Ca^{2+}]$ elevation, is less effective at generating spontaneous Ca^{2+} sparks compared to those that are randomly occurring (compare **Figure 11** and **Figure 14** in Supplementary Materials), such as that brought about by IP_3Rs. Mechanistically, the stochasticity of this "leak" permits some refilling of the JSR prior to an upcoming release, thus generating relatively larger Ca^{2+} fluxes that sporadically elevate dyadic $[Ca^{2+}]$ to levels higher than when a constant "leak" flux is present (compare **Figure 12** and **Figure 15** in Supplementary Materials). The presence of these larger, albeit intermittent, elevations in dyadic $[Ca^{2+}]$ increases the probability that a higher number of RyRs are simultaneously activated due to the super-linear dependence of RyR opening probability on $[Ca^{2+}]$ (see Section 7.2 of Supplementary Materials), significantly increasing the successful formation of spontaneous Ca^{2+} sparks. Increasing the magnitude of this stochastic "leak" flux expectedly increased the occurrence of spontaneous Ca^{2+} spark events. Altogether, our results support the notion that IICR via IP_3Rs expressed in dyads increases the propensity for RyR-mediated Ca^{2+} spark formation by elevating dyadic $[Ca^{2+}]$. However, the stochasticity of IP_3R gating is key to this outcome.

Our findings have important implications about the wider role of IP_3Rs in cardiomyocytes. As we show that IICR increases the probability of Ca^{2+} spark events by raising dyadic $[Ca^{2+}]$, this mechanism may provide a means to activate RyR clusters that are usually "silent" during ECC. This recruitment of RyR clusters can potentially explain the enhanced Ca^{2+} transient amplitude observed in some studies under conditions of IP_3R stimulation (7–11). Indeed, in a recent study in which a dyadic Ca^{2+} reporter was employed, IP_3R activation was found to result in an increase in the number of dyads recruited during ECC (15). In diseased cardiomyocytes, the greater expression of IP_3Rs (8,12) may also suggest a compensatory mechanism for the increased decoupling of RyRs from LTCCs due to T-tubule degradation (35,36) to rescue Ca^{2+} spark formation. However, IICR in dyads could also contribute to increased spontaneous Ca^{2+} release events in cardiomyocytes, which can have arrhythmogenic

consequences (7–11). Furthermore, our simulations showing a progressive decrease in JSR [Ca^{2+}] with increasing IP_3R numbers (second row of **Figure 3**A) also supports an IP_3R function proposed by (34) where an IP_3R overexpression increase Ca^{2+} leaks that fine tune SR levels, thereby protecting against arrhythmias.

4.2 Model limitations and implications

We developed a 1D spatial model of a dyad that reproduced all major characteristics of a Ca^{2+} spark. This enabled its utilization in conducting a qualitative investigation into the influence of IP_3R activity on the dynamics of Ca^{2+} sparks in the dyad. While computationally less expensive, the reduced order of our model from 3D to 1D requires simplifying assumptions that presents several limitations which we discuss below.

4.2.1 Arbitrary RyR and IP_3R Placement

In our model, we chose to fix the number of RyRs in a cluster at 15 based on recent estimates obtained from super resolution imaging data (25–27). Since similar data on IP_3R clusters is unavailable in the literature, the number of IP_3Rs in a cluster is varied to illustrate the effect of increased IP_3R presence on the same RyR cluster. These clusters are then arbitrarily placed in elements of the dyadic region as shown in **Figure 1**. Results presented throughout this study is based on simulations of the model with this specific arrangement of RyRs and IP_3Rs. However, simulations that were performed with randomly determined placement of RyRs and IP_3Rs in the dyadic region with all else kept constant qualitatively reproduced similar results as that shown in **Figure 2** (see **Figure 16** in Supplementary Materials).

The 1D nature of our model precludes our ability to place each RyR in its own element in 3D space such that it can detect Ca^{2+} that has diffused from other RyRs in the cluster. RyRs and IP_3Rs that belong to the same cluster are placed in one element such that all Ca^{2+} channels in that element are assumed to detect the same dyadic [Ca^{2+}]. Similar assumptions have also been employed in previous modelling studies simulating Ca^{2+} sparks (20,37,38). While we acknowledge that developing models of higher dimensions permits one to incorporate the spatial arrangement of individual RyRs in the dyad, which influences Ca^{2+} spark fidelity (17,27), our reduced-order model is sufficient for our purposes of illustrating the effect of IP_3R activity on Ca^{2+} spark dynamics and derive an underlying mechanism for its increased occurrence in the dyad.

4.2.2 Visualisation of Ca^{2+} Spark Fluorescence

Ca^{2+} spark characteristics obtained from experiments are derived from the fluorescence measurement of indicator dyes. To corroborate experimental observations with modelling results, modelling studies incorporate the reaction kinetics of the indicator dye to concurrently simulate the fluorescence of the indicator dye along with the underlying change in [Ca^{2+}]. Although the reaction kinetics between Ca^{2+} and the indicator dye Fluo-4 was included in our model, we could not reliably corroborate its simulated fluorescence with experimental measurements, which show that Ca^{2+} spark amplitudes (in terms of dye fluorescence) are unchanged when IP_3Rs are stimulated (15).

We find that the rise in dyadic [Ca^{2+}] during a Ca^{2+} spark saturates the indicator dye, resulting in a plateau of the fluorescence trace (see **Figure 9**A in Supplementary Materials). Previous modelling and experimental studies have established that [Ca^{2+}] in microdomains such as dyads can be elevated to levels exceeding 20 times of that in the bulk cytosol during a cell-wide Ca^{2+} release (17,20,21,28,39), which is substantially in excess of the [Ca^{2+}] levels accurately reported by Fluo-4. This potentially explains the plateau of the fluorescence trace during a Ca^{2+} spark. Consequently, any change in [Ca^{2+}] elicited by IP_3 would thus be obscured – our model's prediction of a decreasing Ca^{2+} spark amplitude with increasing IICR may even be experimentally undetectable by dye fluorescence. However, we also partly attribute this saturation to the 1D geometry of our model – restriction of species' diffusion to

one dimension. Hence, our 1D model precludes a realistic visualisation of Ca^{2+} sparks as they would be experimentally observed. We acknowledge this as a limitation of our model.

Nevertheless, the Ca^{2+} dynamics associated with Ca^{2+} sparks simulated by our model (**Figure 3**A) agree with previous experimental and model findings. It is hence well suited for our purposes of investigating the functional interactions between IP_3Rs and RyRs, where knowing the concentrations and dynamics of Ca^{2+} within the dyad are required.

5 Conclusions

By incorporating the behaviour of both RyRs and IP_3Rs in our 1D model of the dyad, we show that the stochastic activity of IP_3Rs elevate dyadic $[Ca^{2+}]$, which sensitizes proximal RyRs toward activation. The colocalization of IP_3Rs with RyRs in the dyad thus increases the propensity for RyR-mediated Ca^{2+} sparks which potentially underlies the ECC-modulating effects seen in ventricular cardiomyocytes treated with G_q agonists. In this regard, further work (experimental and modelling) is needed to link our findings of IP_3R-influenced Ca^{2+} spark formation to multiscale whole-cell cardiomyocyte models incorporating IP_3 signalling (40) and Ca^{2+} cycling (41,42) to elucidate its overall impact on global cytosolic Ca^{2+} transient dynamics and ECC (43,44).

Acknowledgements

This research was supported in part by the Australian Government through the Australian Research Council Discovery Projects funding scheme (project DP170101358) to EJC and VR, the Australian Research Council Centre of Excellence in Convergent Bio-Nano Science and Technology (project CE140100036) to EJC, the KU Leuven Global PhD Partnerships with The University of Melbourne Grant (GPUM/21/036) to VR and HLR, and The University of Melbourne's Research Computing Services and the Petascale Campus Initiative. HLR wishes to acknowledge financial support from the Research Foundation Flanders (FWO) through Project Grant G08861N and Odysseus programme Grant 90663. JC would like to thank Dr Pengxing Cao for the useful discussions on IP_3R modelling. S.T.J. is supported by the Australian Research Council (Project No. DE200100988).

6 Reference

1. Bers DM. Cardiac excitation–contraction coupling. Nature. 2002 Jan;415(6868):198–205.

2. Wang SQ, Song LS, Lakatta EG, Cheng H. Ca2+ signalling between single L-type Ca2+ channels and ryanodine receptors in heart cells. Nature. 2001 Mar;410(6828):592–6.

3. Cheng H, Lederer WJ, Cannell MB. Calcium Sparks: Elementary Events Underlying Excitation-Contraction Coupling in Heart Muscle. Science. 1993;262(5134):740–4.

4. Lipp P, Laine M, Tovey SC, Burrell KM, Berridge MJ, Li W, et al. Functional InsP3 receptors that may modulate excitation–contraction coupling in the heart. Current Biology. 2000 Aug 1;10(15):939-S1.

5. Foskett JK, White C, Cheung KH, Mak DOD. Inositol Trisphosphate Receptor Ca2+ Release Channels. Physiological Reviews. 2007 Apr 1;87(2):593–658.

6. Berridge MJ. The Inositol Trisphosphate/Calcium Signaling Pathway in Health and Disease. Physiological Reviews. 2016 Oct 1;96(4):1261–96.

7. Signore S, Sorrentino A, Ferreira-Martins J, Kannappan R, Shafaie M, Del Ben F, et al. Inositol 1, 4, 5-Trisphosphate Receptors and Human Left Ventricular Myocytes. Circulation. 2013 Sep 17;128(12):1286–97.

8. Harzheim D, Movassagh M, Foo RSY, Ritter O, Tashfeen A, Conway SJ, et al. Increased InsP3Rs in the junctional sarcoplasmic reticulum augment Ca2+ transients and arrhythmias associated with cardiac hypertrophy. PNAS. 2009 Jul 7;106(27):11406–11.

9. Nakayama H, Bodi I, Maillet M, DeSantiago J, Domeier TL, Mikoshiba K, et al. The IP3 Receptor Regulates Cardiac Hypertrophy in Response to Select Stimuli. Circulation Research. 2010 Sep 3;107(5):659–66.

10. Proven A, Roderick HL, Conway SJ, Berridge MJ, Horton JK, Capper SJ, et al. Inositol 1,4,5-trisphosphate supports the arrhythmogenic action of endothelin-1 on ventricular cardiac myocytes. Journal of Cell Science. 2006 Aug 15;119(16):3363–75.

11. Domeier TL, Zima AV, Maxwell JT, Huke S, Mignery GA, Blatter LA. IP3 receptor-dependent Ca2+ release modulates excitation-contraction coupling in rabbit ventricular myocytes. American Journal of Physiology-Heart and Circulatory Physiology. 2008 Feb;294(2):H596–604.

12. Harzheim D, Talasila A, Movassagh M, Foo RSY, Figg N, Bootman MD, et al. Elevated InsP3R expression underlies enhanced calcium fluxes and spontaneous extra-systolic calcium release events in hypertrophic cardiac myocytes. Channels. 2010 Jan 1;4(1):67–71.

13. Moschella MC, Marks AR. Inositol 1,4,5-trisphosphate receptor expression in cardiac myocytes. Journal of Cell Biology. 1993 Mar 1;120(5):1137–46.

14. Gilbert G, Demydenko K, Dries E, Puertas RD, Jin X, Sipido K, et al. Calcium Signaling in Cardiomyocyte Function. Cold Spring Harb Perspect Biol. 2020 Mar 1;12(3):a035428.

15. Demydenko K, Sipido KR, Roderick HL. Ca2+ release via InsP3Rs enhances RyR recruitment during Ca2+ transients by increasing dyadic [Ca2+] in cardiomyocytes. Journal of Cell Science [Internet]. 2021 Jul 22 [cited 2021 Sep 22];134(14). Available from: https://doi.org/10.1242/jcs.258671

16. Wullschleger M, Blanch J, Egger M. Functional local crosstalk of inositol 1,4,5-trisphosphate receptor- and ryanodine receptor-dependent Ca2+ release in atrial cardiomyocytes. Cardiovascular Research. 2017 Apr 1;113(5):542–52.

17. Walker MA, Williams GSB, Kohl T, Lehnart SE, Jafri MS, Greenstein JL, et al. Superresolution Modeling of Calcium Release in the Heart. Biophysical Journal. 2014 Dec 16;107(12):3018–29.

18. Picht E, Zima AV, Shannon TR, Duncan AM, Blatter LA, Bers DM. Dynamic Calcium Movement Inside Cardiac Sarcoplasmic Reticulum During Release. Circulation Research. 2011 Apr 1;108(7):847–56.

19. Zima AV, Picht E, Bers DM, Blatter LA. Termination of Cardiac Ca2+ Sparks. Circulation Research. 2008 Oct 10;103(8):e105–15.

20. Williams GSB, Chikando AC, Tuan HTM, Sobie EA, Lederer WJ, Jafri MS. Dynamics of Calcium Sparks and Calcium Leak in the Heart. Biophysical Journal. 2011 Sep 21;101(6):1287–96.

21. Cannell MB, Kong CHT, Imtiaz MS, Laver DR. Control of Sarcoplasmic Reticulum Ca2+ Release by Stochastic RyR Gating within a 3D Model of the Cardiac Dyad and Importance of Induction Decay for CICR Termination. Biophysical Journal. 2013 May 21;104(10):2149–59.

22. Siekmann I, Wagner LE, Yule D, Crampin EJ, Sneyd J. A Kinetic Model for Type I and II IP3R Accounting for Mode Changes. Biophysical Journal. 2012 Aug 22;103(4):658–68.

23. Cao P, Tan X, Donovan G, Sanderson MJ, Sneyd J. A Deterministic Model Predicts the Properties of Stochastic Calcium Oscillations in Airway Smooth Muscle Cells. PLOS Computational Biology. 2014 Aug 14;10(8):e1003783.

24. Cao P, Donovan G, Falcke M, Sneyd J. A Stochastic Model of Calcium Puffs Based on Single-Channel Data. Biophysical Journal. 2013 Sep 3;105(5):1133–42.

25. Baddeley D, Jayasinghe ID, Lam L, Rossberger S, Cannell MB, Soeller C. Optical single-channel resolution imaging of the ryanodine receptor distribution in rat cardiac myocytes. PNAS. 2009 Dec 29;106(52):22275–80.

26. Shen X, van den Brink J, Hou Y, Colli D, Le C, Kolstad TR, et al. 3D dSTORM imaging reveals novel detail of ryanodine receptor localization in rat cardiac myocytes. The Journal of Physiology. 2019;597(2):399–418.

27. Kolstad TR, van den Brink J, MacQuaide N, Lunde PK, Frisk M, Aronsen JM, et al. Ryanodine receptor dispersion disrupts Ca2+ release in failing cardiac myocytes. Dietz HC, Vunjak-Novakovic G, editors. eLife. 2018 Oct 30;7:e39427.

28. Smith GD, Keizer JE, Stern MD, Lederer WJ, Cheng H. A Simple Numerical Model of Calcium Spark Formation and Detection in Cardiac Myocytes. Biophysical Journal. 1998 Jul 1;75(1):15–32.

29. Rüdiger S, Shuai JW, Huisinga W, Nagaiah C, Warnecke G, Parker I, et al. Hybrid Stochastic and Deterministic Simulations of Calcium Blips. Biophysical Journal. 2007 Sep 15;93(6):1847–57.

30. Laver DR, Kong CHT, Imtiaz MS, Cannell MB. Termination of calcium-induced calcium release by induction decay: An emergent property of stochastic channel gating and molecular scale architecture. Journal of Molecular and Cellular Cardiology. 2013 Jan 1;54:98–100.

31. Higazi DR, Fearnley CJ, Drawnel FM, Talasila A, Corps EM, Ritter O, et al. Endothelin-1-Stimulated InsP3-Induced Ca2+ Release Is a Nexus for Hypertrophic Signaling in Cardiac Myocytes. Molecular Cell. 2009 Feb 27;33(4):472–82.

32. Wagner LE, Yule DI. Differential regulation of the $InsP_3$ receptor type-1 and -2 single channel properties by $InsP_3$, Ca^{2+} and ATP. J Physiol. 2012 Jul 15;590(14):3245–59.

33. Chen H, Valle G, Furlan S, Nani A, Gyorke S, Fill M, et al. Mechanism of calsequestrin regulation of single cardiac ryanodine receptor in normal and pathological conditions. Journal of General Physiology. 2013 Jul 15;142(2):127–36.

34. Blanch i Salvador J, Egger M. Obstruction of ventricular Ca2+-dependent arrhythmogenicity by inositol 1,4,5-trisphosphate-triggered sarcoplasmic reticulum Ca2+ release. The Journal of Physiology. 2018;596(18):4323–40.

35. Pinali C, Malik N, Davenport JB, Allan LJ, Murfitt L, Iqbal MM, et al. Post-Myocardial Infarction T-tubules Form Enlarged Branched Structures With Dysregulation of Junctophilin-2 and Bridging Integrator 1 (BIN-1). Journal of the American Heart Association. 2017 May 4;6(5):e004834.

36. Guo A, Zhang C, Wei S, Chen B, Song LS. Emerging mechanisms of T-tubule remodelling in heart failure. Cardiovasc Res. 2013 May 1;98(2):204–15.

37. Groff JR, Smith GD. Calcium-dependent inactivation and the dynamics of calcium puffs and sparks. Journal of Theoretical Biology. 2008 Aug 7;253(3):483–99.

38. Macquaide N, Tuan HTM, Hotta J ichi, Sempels W, Lenaerts I, Holemans P, et al. Ryanodine receptor cluster fragmentation and redistribution in persistent atrial fibrillation enhance calcium release. Cardiovascular Research. 2015 Dec 1;108(3):387–98.

39. Acsai K, Antoons G, Livshitz L, Rudy Y, Sipido KR. Microdomain [Ca2+] near ryanodine receptors as reported by L-type Ca2+ and Na+/Ca2+ exchange currents. The Journal of Physiology. 2011;589(10):2569–83.

40. Cooling M, Hunter P, Crampin EJ. Modeling Hypertrophic IP3 Transients in the Cardiac Myocyte. Biophysical Journal. 2007 Nov 15;93(10):3421–33.

41. Hunt H, Tilūnaitė A, Bass G, Soeller C, Roderick HL, Rajagopal V, et al. Ca2+ Release via IP3 Receptors Shapes the Cardiac Ca2+ Transient for Hypertrophic Signaling. Biophys J. 2020 Sep 15;119(6):1178–92.

42. Vierheller J, Neubert W, Falcke M, Gilbert S, Chamakuri N. A multiscale computational model of spatially resolved calcium cycling in cardiac myocytes: from detailed cleft dynamics to the whole cell concentration profiles. Frontiers in Physiology [Internet]. 2015 [cited 2022 Feb 15];6. Available from: https://www.frontiersin.org/article/10.3389/fphys.2015.00255

43. Crampin EJ, Smith NP, Hunter PJ. Multi-scale modelling and the IUPS physiome project. Histochem J. 2004 Sep 1;35(7):707–14.

44. Terkildsen JR, Niederer S, Crampin EJ, Hunter P, Smith NP. Using Physiome standards to couple cellular functions for rat cardiac excitation–contraction. Experimental Physiology. 2008;93(7):919–29.

45. Bers DM. Sources and Sinks of Activator Calcium. In: Bers DM, editor. Excitation-Contraction Coupling and Cardiac Contractile Force [Internet]. Dordrecht: Springer Netherlands; 2001 [cited 2022 Mar 16]. p. 39–62. Available from: https://doi.org/10.1007/978-94-010-0658-3_3

46. Tran K, Smith NP, Loiselle DS, Crampin EJ. A Thermodynamic Model of the Cardiac Sarcoplasmic/Endoplasmic Ca2+ (SERCA) Pump. Biophysical Journal. 2009 Mar 4;96(5):2029–42.

7 Supplementary Materials

7.1 Parameter Values

Values for every parameter used to simulate the Ca^{2+} reaction diffusion in our model are shown in Table 1 and Table 2. All values are adapted directly from (17) except where otherwise indicated.

Table 1. Parameter values of all species involved in reaction diffusion.

Species	Concentration (μM)	Diffusivity, $\mathcal{D}$ ($\mu m^2/ms$)	Forward Reaction Rate, k_{on} ($\mu M^{-1}ms^{-1}$)	Backward Reaction Rate, k_{off} (ms^{-1})
$[Ca^{2+}]_c$	0.1 (initial)	0.22	-	-
$[Ca^{2+}]_{JSR}$	1000 (initial)	0.35[1]	-	-
$[Ca^{2+}]_{NSR}$	1000 (initial)	0.06	-	-
ATP	455 (total)	0.14	0.225	45
CaM	24 (total)	0.025	0.025	0.238
Fluo-4	100 (total)	0.042	0.0488[1]	0.0439[1]
TnC	70 (total)	0	0.039	0.02
CSQ	30000 (total)	0	0.1	63.8

Table 2. Parameter values involved in calculating Ca^{2+}-handling protein fluxes and JSR refill.

Ca^{2+}-Handling Protein	Parameter	Description	Value
RyR	g_{RyR}	RyR Ca^{2+} release flux rate	2.8 ms^{-1} [2]
IP_3R	g_{IP_3R}	IP_3R Ca^{2+} release flux rate	0.982 ms^{-1} [3]
SERCA	A_p	SERCA concentration	75 μM[4]
	K_{D_c}	SERCA sensitivity to $[Ca^{2+}]_c$	910 μM
	$K_{D_{SR}}$	SERCA sensitivity to $[Ca^{2+}]_{NSR}$	2240 μM
JSR	g_{refill}	JSR refill flux rate	0.20 ms^{-1} [5]

7.2 RyR Model

The RyR model used in our simulations is directly adapted from that developed by (21) of the rat. The gating of each RyR is modelled as a 2-state Markov process (**Figure 5**).

$$CLOSE \underset{k_{close}}{\overset{k_{open}}{\rightleftharpoons}} OPEN$$

Figure 5. State diagram of RyR model. *Developed by (21), this model of the RyR consists of 2 states, denoted by OPEN and CLOSE, that the RyR transitions between at transition rates k_{open} and k_{close}.*

Where the Ca^{2+}-dependent transition rates, in ms, between the states, are expressed as,

$$k_{open} = \min(3.17 \times 10^2 \times [Ca^{2+}]_c^{2.8}, 0.7)$$

[1] Value taken from (21)

[2] Adjusted to give a realistic Ca^{2+} spark profile

[3] Value calculated as 2.85 times lower than g_{RyR} as Ca^{2+} conductance of IP_3Rs is estimated to be ~2.85 lower than RyRs (5)

[4] Value taken from (45)

[5] Adjusted to give a $[Ca^{2+}]_{JSR}$ exponential recovery time constant of ~130 ms as in (17–19)

$$k_{close} = \max(0.25 \times [Ca^{2+}]_c^{-0.5}, 0.9)$$

7.3 IP_3R Model

IP_3Rs in our simulations are modelled after that developed by (24) who modified the park-drive model (22) to account for unsteady state kinetics of IP_3Rs when subject to constantly changing concentrations of regulatory ligands (in this case, Ca^{2+}). The gating of each IP_3R is modelled as a 6-state Markov process (**Figure 6**).

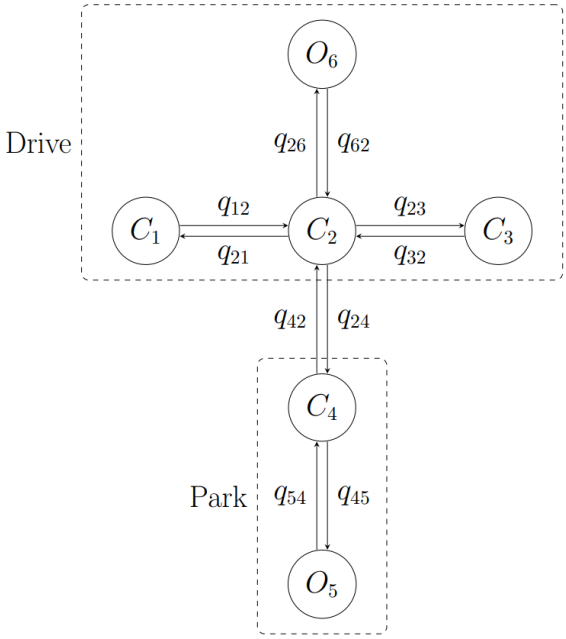

Figure 6. State diagram of IP_3R model. *Developed by (22), this model of the IP_3R consists of six states that are categorised into two modes of activity: Park and Drive. Park mode is when the channel is at the closed state C_4 or open state O_5. Drive mode is when the channel is at closed states C_1, C_2, C_3 or open state O_6. State transition rates are denoted by q. Intramodal transition rates are constants whereas intermodal transition rates are dependent on ligand concentration.*

Intramodal transition rates are constants whose values are shown in Table 3 below,

Table 3. Constant IP_3R2 transition rates. Values obtained from (22).

IP_3R2 State Transition Rate	Value (ms^{-1})
q_{12}	1.14
q_{21}	0.0958
q_{23}	0.0047
q_{32}	0.0119
q_{26}	10.100
q_{62}	3.270
q_{45}	0.0041
q_{54}	3.420

Intermodal transition rates q_{24} and q_{42} are ligand-dependent whose expressions are given by,

$$q_{24} = a_{24} + V_{24}(1 - m_{24}h_{24})$$
$$q_{42} = a_{42} + V_{42}m_{42}h_{42}$$

Where variables a, V, m, and h are functions of concentrations of ligands IP_3, $[IP_3]$ and Ca^{2+}, $[Ca^{2+}]$ and are given by the following expressions. These expressions take a similar form to that in (23,24).

$$a_{24} = \frac{100}{[IP_3]^{54.5} + 0.923^{54.5}}$$
$$a_{42} = 1.0 + \frac{24.5}{[IP_3]^{2.8} + 3.4^{2.8}}$$
$$V_{24} = 200.3 + \frac{24.1[IP_3]^{54.9}}{[IP_3]^{54.9} + 46.8^{54.9}}$$
$$V_{42} = 60.0 + \frac{745.0}{[IP_3]^{8.6} + 1.0^{8.6}}$$
$$m_{24} = \frac{[Ca^{2+}]^{n_{24}}}{k_{24}^{n_{24}} + [Ca^{2+}]^{n_{24}}}$$
$$m_{42} = \frac{[Ca^{2+}]^{n_{42}}}{k_{42}^{n_{42}} + [Ca^{2+}]^{n_{42}}}$$
$$h_{24} = \frac{k_{-24}^{n_{-24}}}{k_{-24}^{n_{-24}} + [Ca^{2+}]^{n_{24}}}$$
$$h_{42} = \frac{k_{-42}^{n_{-42}}}{k_{-42}^{n_{-42}} + [Ca^{2+}]^{n_{42}}}$$
$$k_{24} = 0.0358$$
$$k_{42} = 0.15$$
$$n_{24} = 9.5$$
$$n_{42} = 5.5$$
$$k_{-24} = 15.9 + \frac{774.2}{[IP_3]^{2.7} + 33.0^{2.7}}$$
$$k_{-42} = 0.8 + \frac{19000}{[IP_3]^{11.6} + 86.8^{11.6}}$$
$$n_{-24} = 1.14 + \frac{1.19[IP_3]^{1.25}}{[IP_3]^{1.25} + 20.7^{1.25}}$$
$$n_{-42} = 1.7 + \frac{37.8}{[IP_3]^{15.1} + 1.2^{15.1}}$$

Coefficients and exponents in expressions of the gating variables stated above are determined by fitting the curve of q_{24} and q_{42} to their known steady state data points. These data points (**Figure 7**A) were previously derived from experimental data by (22) and are specific to IP_3R2. We chose to fit our plots of q_{24} and q_{42} to data points obtained at 1 µM and 10 µM [IP_3] and 5 mM [ATP] as there were more data points that we could fit our curves to and also because 5 mM [ATP] was closer to the physiological [ATP] in cardiomyocytes. The resultant fitted curves of q_{24} and q_{42} as a function of [Ca^{2+}] and [IP_3] are shown in **Figure 7**A. q_{24} and q_{42} at 0.15 µM [IP_3], the concentration at which IP_3 is fixed in all our simulations, were then extrapolated from these expressions and is shown in **Figure 7**B. The corresponding open probability curves calculated (**Figure 7**C) are comparable to those obtained from experiments (32).

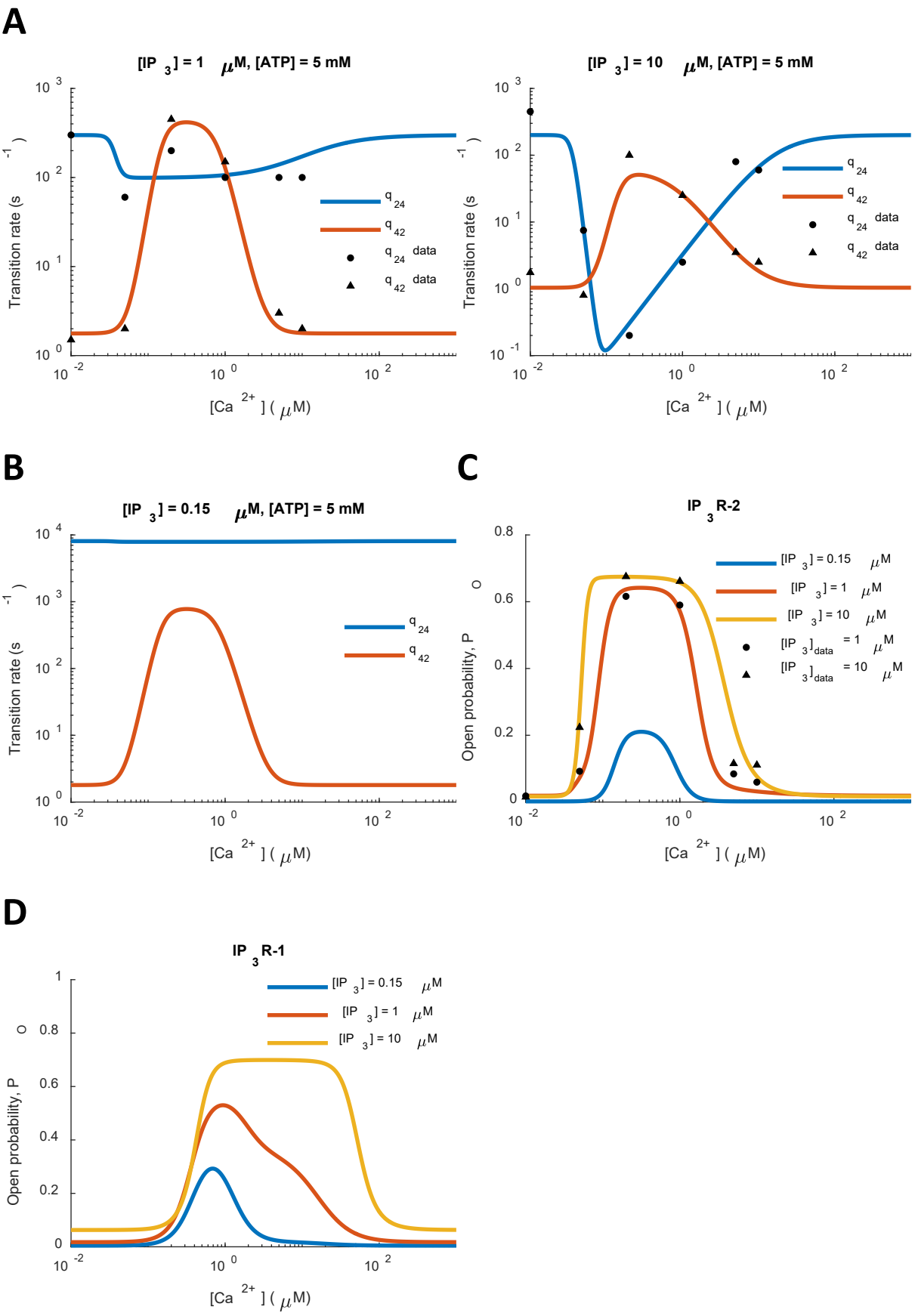

Figure 7. Intermodal transition rates q_{24} and q_{42} vs [Ca²⁺] and open probability curves of IP₃R2. A: *q_{24} and q_{42} vs [Ca²⁺] curves of IP₃R- at [IP₃] = 1 and 10 μM. Curves were obtained by tuning coefficients and exponents in expressions for variables a, V, m, h, and k to give curves of best fit for experimentally obtained q_{24} and q_{42} data points from (22).* ***B:*** *q_{24} and q_{42} vs*

*[Ca^{2+}] curves at [IP_3] = 0.15 µM. These curves were obtained by extrapolating from expressions used to plot the same curves in **A** as no experimental data points were available at this [IP_3]. **C:** The corresponding open probability, P_O, vs [Ca^{2+}] curve of IP_3R2. **D:** P_O vs [Ca^{2+}] curve of the IP_3R1 model developed in (23).*

To account for IP_3R2 gating behaviour in an environment where [Ca^{2+}] is constantly changing, the non-steady state kinetics of the Ca^{2+}-dependent gating variables were assumed to obey the differential equation of the form below (24),

$$\frac{dG}{dt} = \lambda_G(G_\infty - G)$$

Where, G represent the current value of gating variables m_{24}, h_{24}, m_{42}, and h_{42} and G_∞ represents the value of the same variables at steady state. λ_G is the equilibrium approach rate whose values are given in Table 4.

Table 4. The equilibrium approach rate for all Ca^{2+}-dependent gating variables. Values are obtained from (23,24).

Equilibrium Approach Rate	Value (ms^{-1})
$\lambda_{m_{24}}$	0.1
$\lambda_{h_{24}}$	0.04
$\lambda_{m_{42}}$	0.1
$\lambda_{h_{42}}$	0.1 when IP_3R is open, 5×10^{-4} when closed

7.4 SERCA Model

The SERCA model implemented and its parameters were directly adapted from (20) which based it on the simplified thermodynamically realistic model developed by (46). The Ca^{2+} uptake flux by SERCA, J_{SERCA}, is given by

$$J_{SERCA} = 2v_{cycle}A_p$$

Where each term is defined as:

$$v_{cycle} = \frac{3.24873 \times 10^{12}K_c^2 + K_c(9.17846 \times 10^6 - 11478.2K_{SR}) - 0.329904K_{SR}}{D_{cycle}}$$

$$D_{cycle} = 0.104217 + 17.293K_{SR} + K_c(1.75583 \times 10^6 + 7.61673 \times 10^6 K_{SR}) + K_c^2(6.08462 \times 10^{11} + 4.50544 \times 10^{11}K_{SR})$$

$$K_c = \left(\frac{[Ca^{2+}]_c}{K_{D_c}}\right)^2$$

$$K_{SR} = \left(\frac{[Ca^{2+}]_{NSR}}{K_{D_{SR}}}\right)^2$$

v_{cycle} corresponds to the cycling rate per SERCA molecule while A_p corresponds to the cytosolic concentration of SERCA molecules. K_{D_c} and $K_{D_{SR}}$ are constants quantifying the sensitivity of SERCA activity to $[Ca^{2+}]_c$ and $[Ca^{2+}]_{NSR}$ respectively. Their values are given in Table 2.

7.5 Ca^{2+} Spark Analysis

Ca^{2+} releases at the dyad are identified as Ca^{2+} sparks when it involves the opening of > 5 RyRs in the dyad. This classification is justified as Ca^{2+} sparks that occur in our simulations typically involve the opening of 12 – 20 RyRs in the dyad. The amplitude and FDHM of Ca^{2+} sparks were then obtained from Ca^{2+} trace of Ca^{2+} spark events using the *findpeaks* function in MATLAB (**Figure 8**B and **Figure 8**C).

A

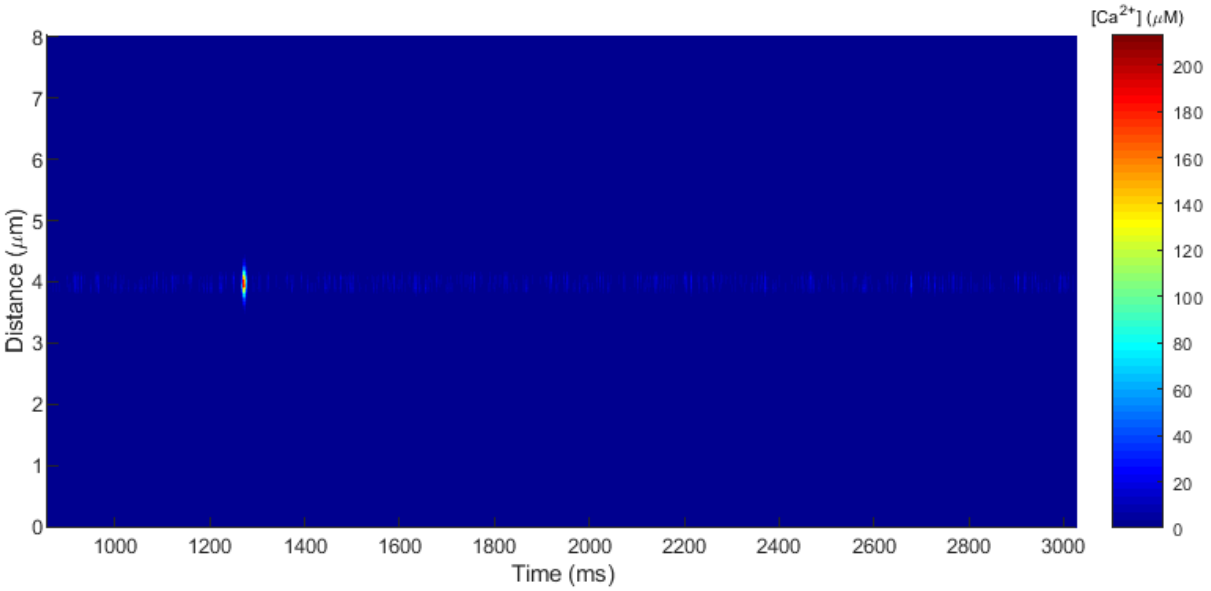
[Ca2+] (μM)
Distance (μm)
Time (ms)

B

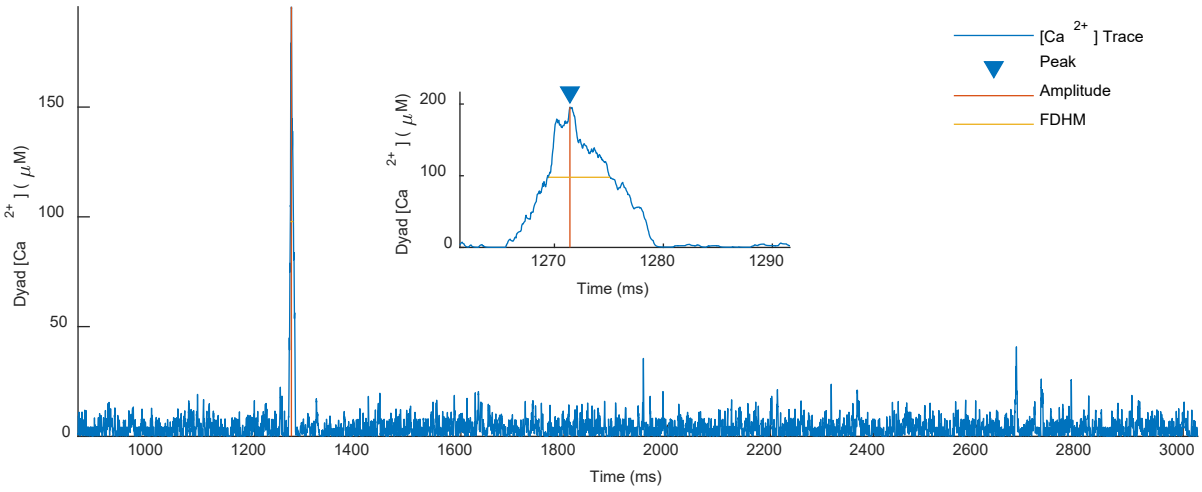
[Ca 2+] Trace
Peak
Amplitude
FDHM
Dyad [Ca 2+] (μM)
Time (ms)

C

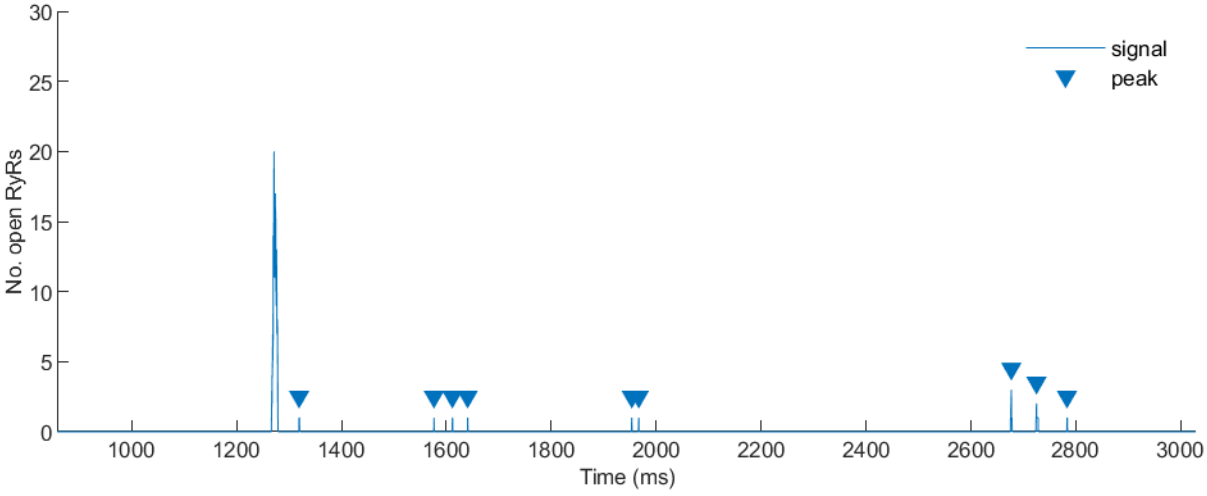
signal
peak
No. open RyRs
Time (ms)

Figure 8. Detection and analysis of Ca^{2+} spark events. A: *The [Ca^{2+}] equivalent of a line scan image of a Ca^{2+} spark.* ***B:*** *Ca^{2+} spark detection and measurement of its amplitude and FDHM. Ca^{2+} sparks detected are denoted by an inverted triangle at its peak [Ca^{2+}]. Inset shows how the amplitude and FDHM of a detected Ca^{2+} spark is measured.* ***C:*** *Detection of spontaneous RyR openings that do not develop into a full Ca^{2+} spark. Full Ca^{2+} spark events were excluded from this detection.*

7.6 Ca^{2+} Spark Fluorescence

Figure 9A shows the simulated fluorescence line scan images and traces from the center of the dyad together with their equivalent [Ca^{2+}] counterpart **Figure 9**B. Due to the 1D nature of our model, we convolved the simulated fluorescence with a 1D Gaussian PSF with a FWHM of 0.41 µm. Notice the plateau in the fluorescence trace of a Ca^{2+} spark that indicates the saturation of the indicator dye (**Figure 9**A). Our simulated fluorescence result shows a similar Ca^{2+} spark amplitude independent of IP_3R activity, which is consistent with experimental data (15). However, we are unable to reliably conclude this as it may be biased by the saturation of the indicator dye.

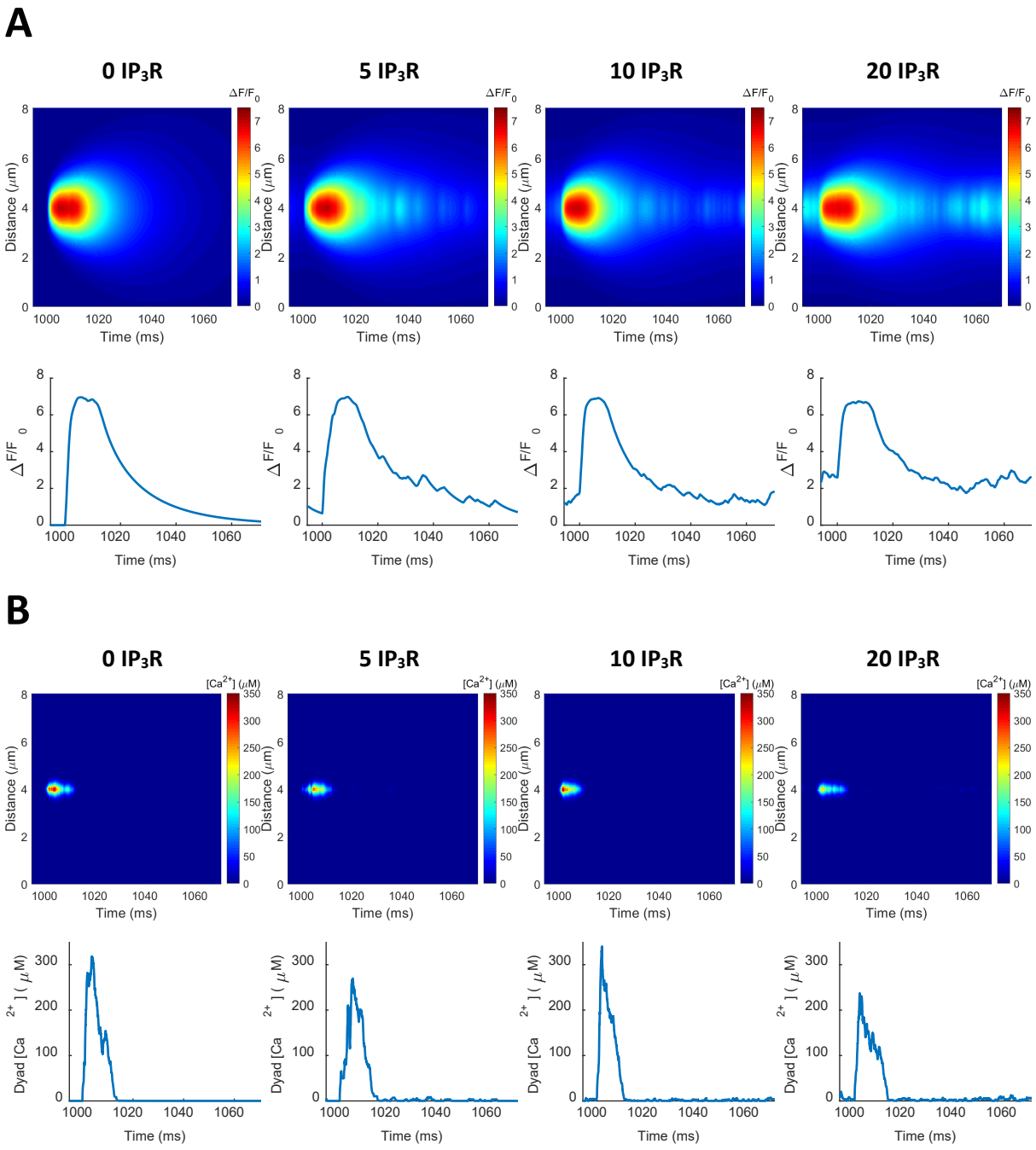

Figure 9. Ca^{2+} spark fluorescence and its underlying $[Ca^{2+}]$. A: *Line scan images of a Ca^{2+} spark and its fluorescence trace taken at the center of the line scan.* ***B:*** *The $[Ca^{2+}]$ equivalent of a line scan image and its $[Ca^{2+}]$ trace taken at the center of the line scan.*

7.7 Mechanism Verification

To verify that the mechanism of the increased propensity of Ca^{2+} spark formation is indeed due to the leak-like function of dyad-localized IP_3Rs that elevates dyadic $[Ca^{2+}]$, we performed simulations with hypothetical Ca^{2+} "leak" fluxes from the JSR to the dyad in place of the IP_3R model. To demonstrate the incremental effect of this "leak", we adjusted its magnitude such that the resulting Ca^{2+} dynamics associated with an LTCC-triggered Ca^{2+} spark is representative of that by our default model (compare **Figure 3** with **Figure 10**A and **Figure 13**A). With this modification to the model, we then performed simulations with no LTCC triggers to show that an increased occurrence of spontaneous Ca^{2+} sparks is correlated to an elevated dyadic $[Ca^{2+}]$, thus verifying this mechanism.

We first performed simulations with a constant Ca^{2+} "leak" flux with the expectation that the number of spontaneous Ca^{2+} spark events would be increased with the magnitude of this "leak". However, the number of spontaneous Ca^{2+} sparks generated was not sufficient for us to draw this conclusion (**Figure 11**). Hence, we repeated the steps detailed above in a subsequent set of simulation with Ca^{2+} fluxes that randomly occur for randomly determined time intervals. This modification recovered the result of our default model configuration (**Figure 14**), demonstrating the importance of stochastic IP_3R gating.

7.7.1 Constant Ca^{2+} Flux

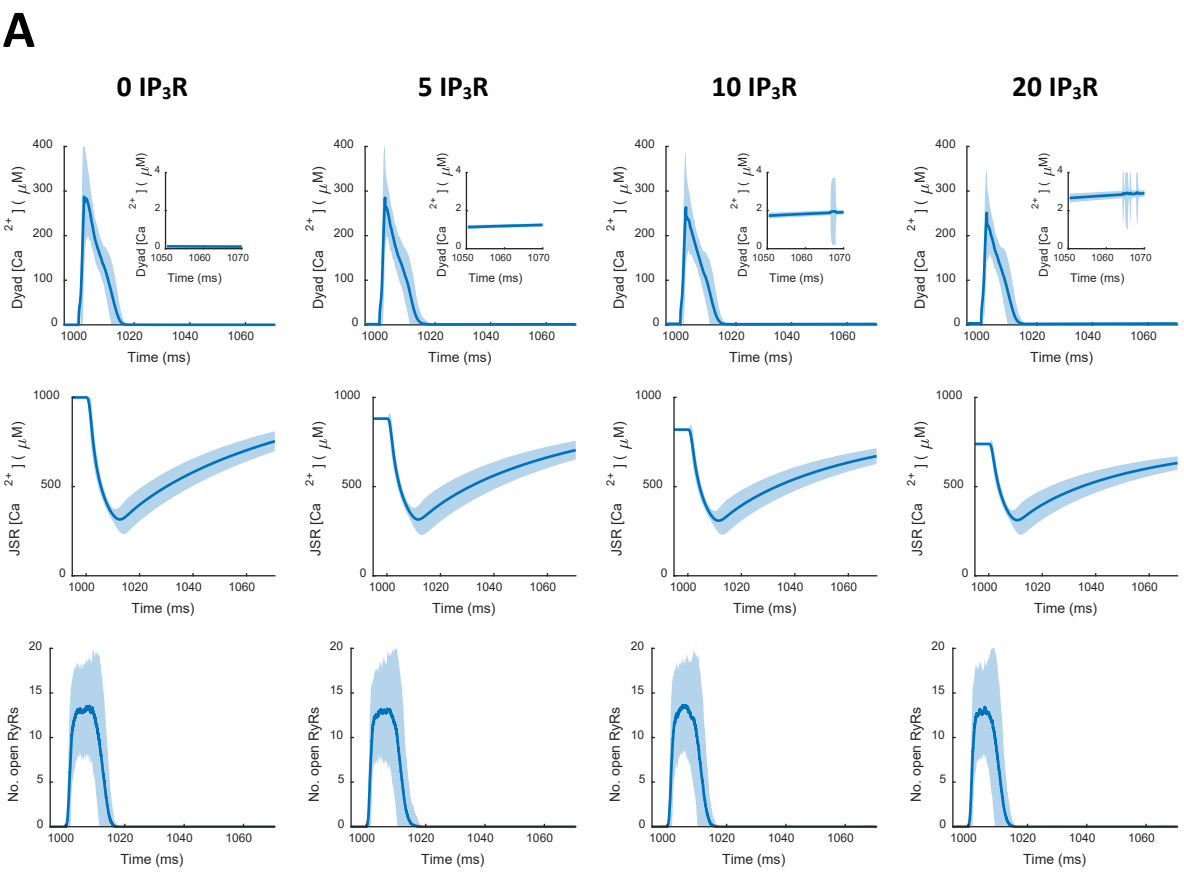

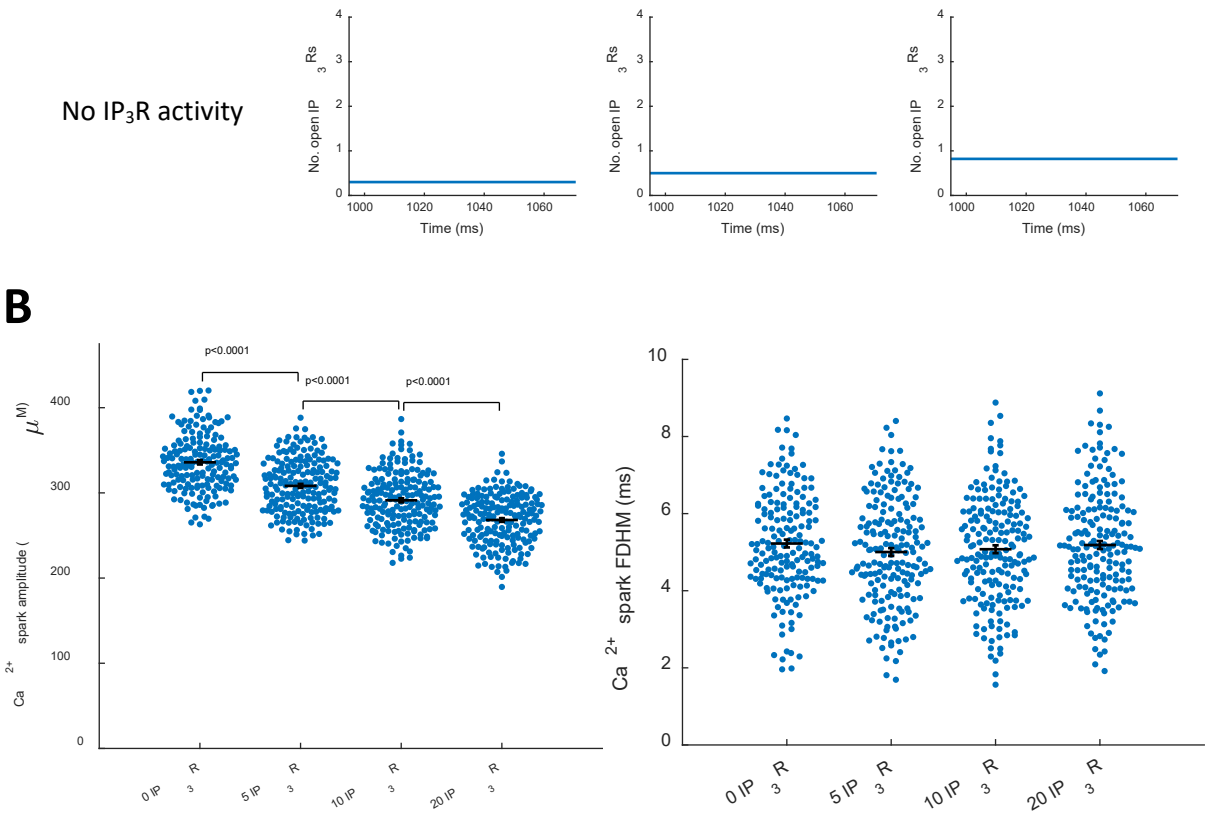

Figure 10. Ca^{2+} dynamics associated with LTCC-initiated Ca^{2+} sparks for simulations with a constant Ca^{2+} "leak" flux at IP_3R-containing elements. A: *From first to fourth row: Time evolution of dyadic [Ca^{2+}] (Insets show an average baseline dyadic [Ca^{2+}] that increases with the equivalent number of IP_3Rs), time evolution of JSR [Ca^{2+}], the number of open RyRs, and the equivalent number of open IP_3Rs associated with a Ca^{2+} spark. The mean and 95% confidence intervals, shown as solid lines and the surrounding shaded region respectively, are obtained from 200 simulations performed for each IP_3R number condition.* ***B:*** *Swarm plots showing a decreasing average Ca^{2+} spark amplitude but unchanged FDHM with increasing equivalent number of IP_3Rs. Analysis by 1 way ANOVA with Tukey-Kramer post hoc test. Data points were obtained from the same 200 simulations as that in **A**.*

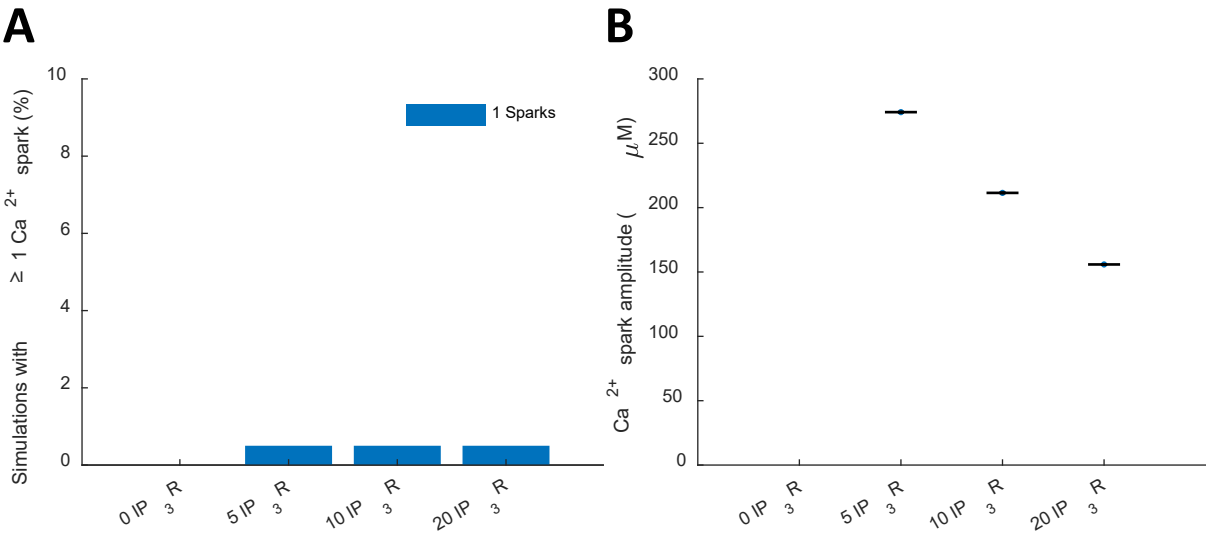

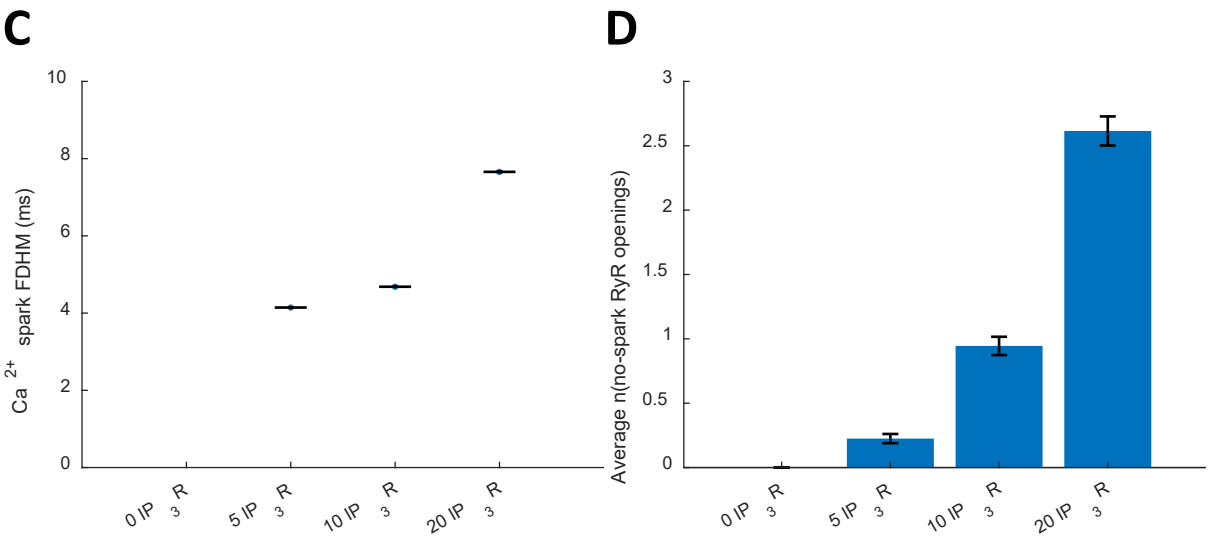

Figure 11. Simulations with constant Ca^{2+} "leak" fluxes from the JSR into the dyad elicited a significantly lower number of spontaneous Ca^{2+} spark events. A: *Percentage of simulations where at least 1 Ca^{2+} spark event spontaneously occurred.* ***B:*** *Swarm plot showing the amplitude of spontaneous Ca^{2+} spark events.* ***C:*** *Swarm plot showing the FDHM of spontaneous Ca^{2+} sparks.* ***D:*** *Average number of RyR opening events that do not lead to a Ca^{2+} spark increases with the equivalent number of IP_3Rs. All results presented in this figure were obtained from 200 simulations for each IP_3R number condition. Insufficient Ca^{2+} spark events were generated to reliably perform a statistical analysis.*

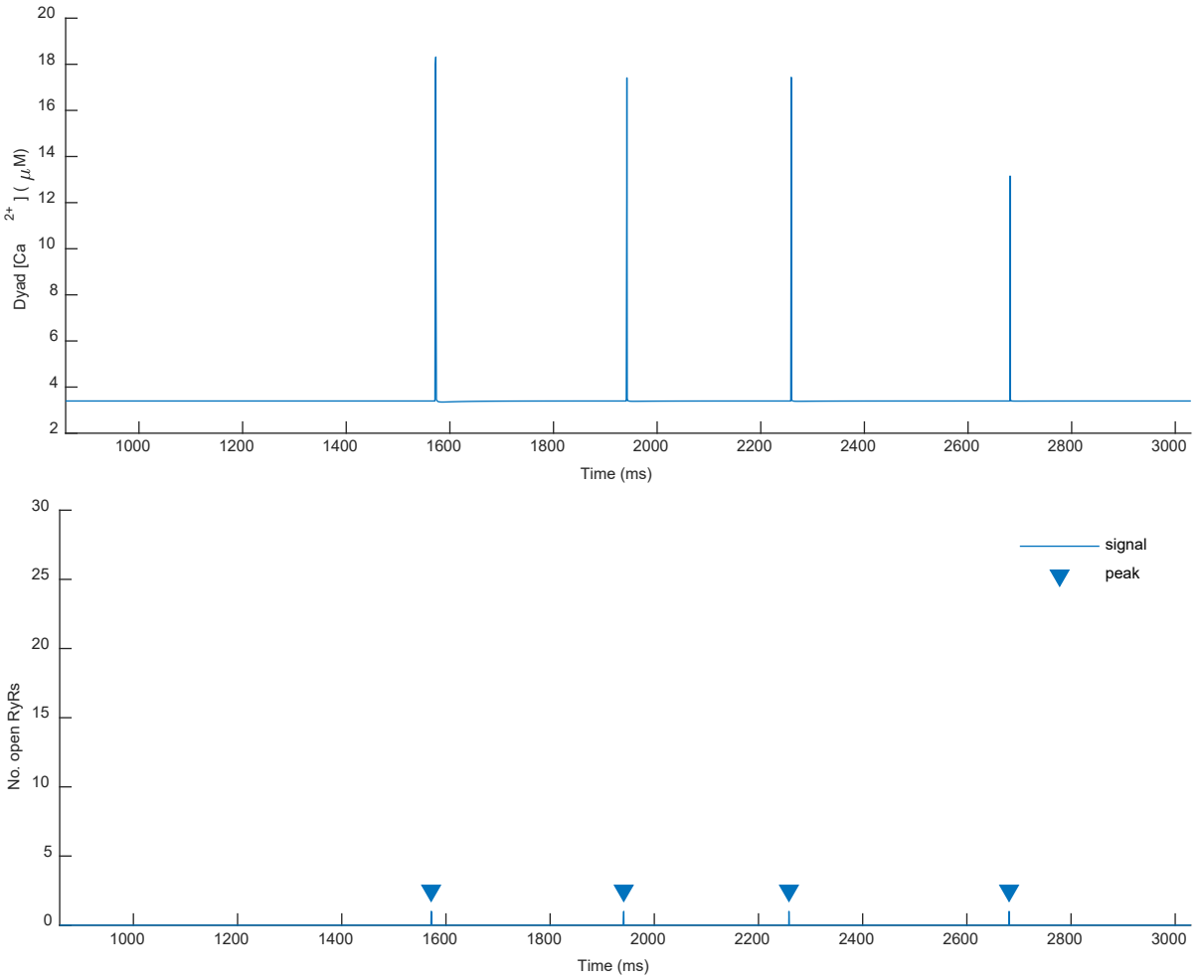

Figure 12. Dyadic [Ca^{2+}] trace of a simulation that has no Ca^{2+} spark events. *Replacing IP_3Rs with a constant JSR Ca^{2+} leak flux leads to a constant dyadic [Ca^{2+}] elevation. Spikes are correlated with eventless RyR openings shown in the lower panel.*

7.7.2 Random Ca^{2+} Flux

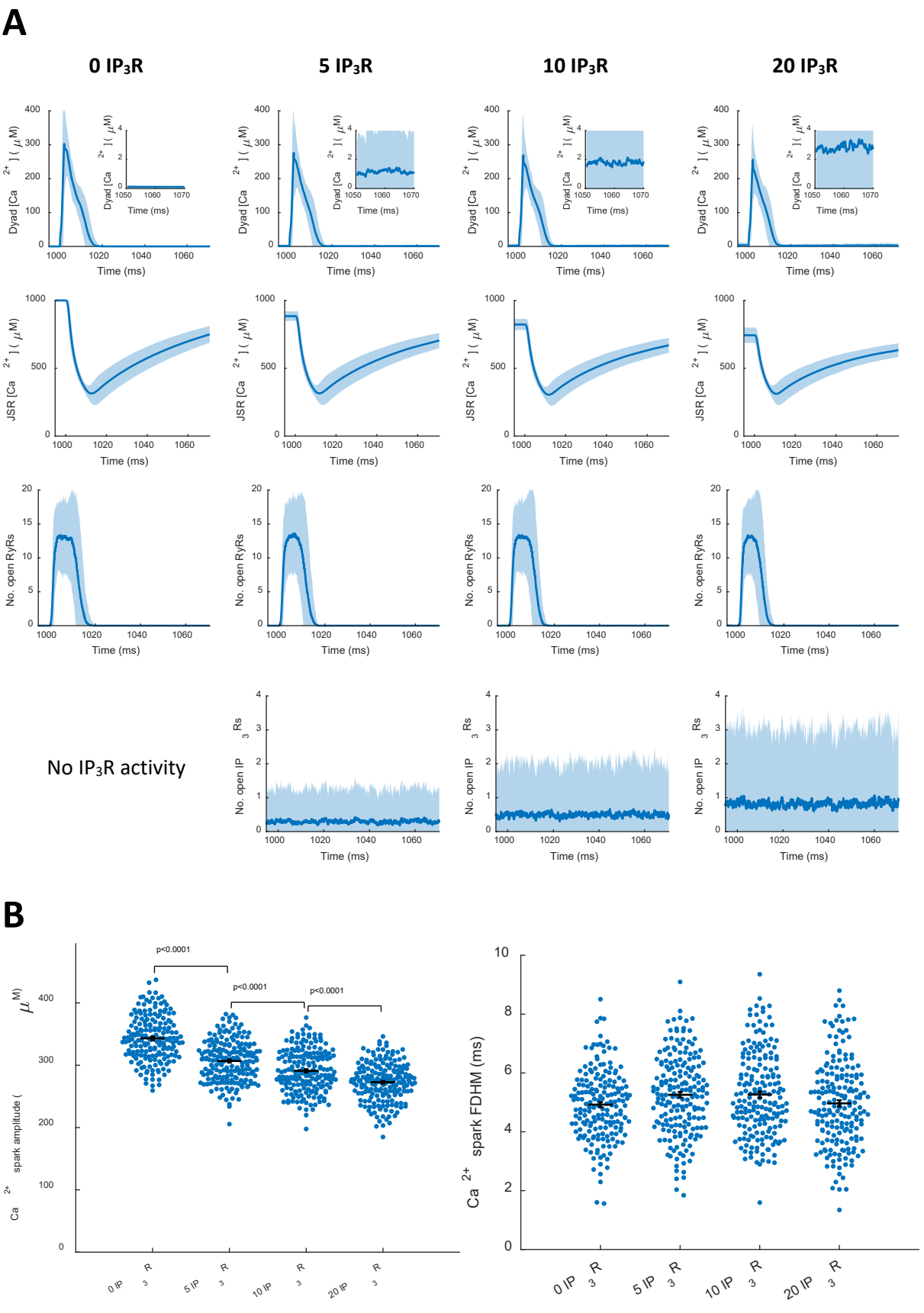

Figure 13. Ca^{2+} dynamics associated with LTCC-initiated Ca^{2+} sparks for simulations with randomly occurring Ca^{2+} "leak" fluxes at IP_3R-containing elements. A: *From first to fourth row: Time evolution of dyadic [Ca^{2+}] (Insets show average baseline*

*dyadic [Ca^{2+}] that increases with the equivalent number of IP_3Rs), time evolution of JSR [Ca^{2+}], the number of open RyRs, and the equivalent number of open IP_3Rs associated with a Ca^{2+} spark. The mean and 95% confidence intervals, shown as solid lines and the surrounding shaded region respectively, are obtained from 200 simulations performed for each IP_3R number condition. **B:** Swarm plots showing a decreasing average Ca^{2+} spark amplitude but unchanged FDHM with increasing equivalent number of IP_3Rs. Analysis by 1 way ANOVA with Tukey-Kramer post hoc test. Data points were obtained from the same 200 simulations as that in **A**.*

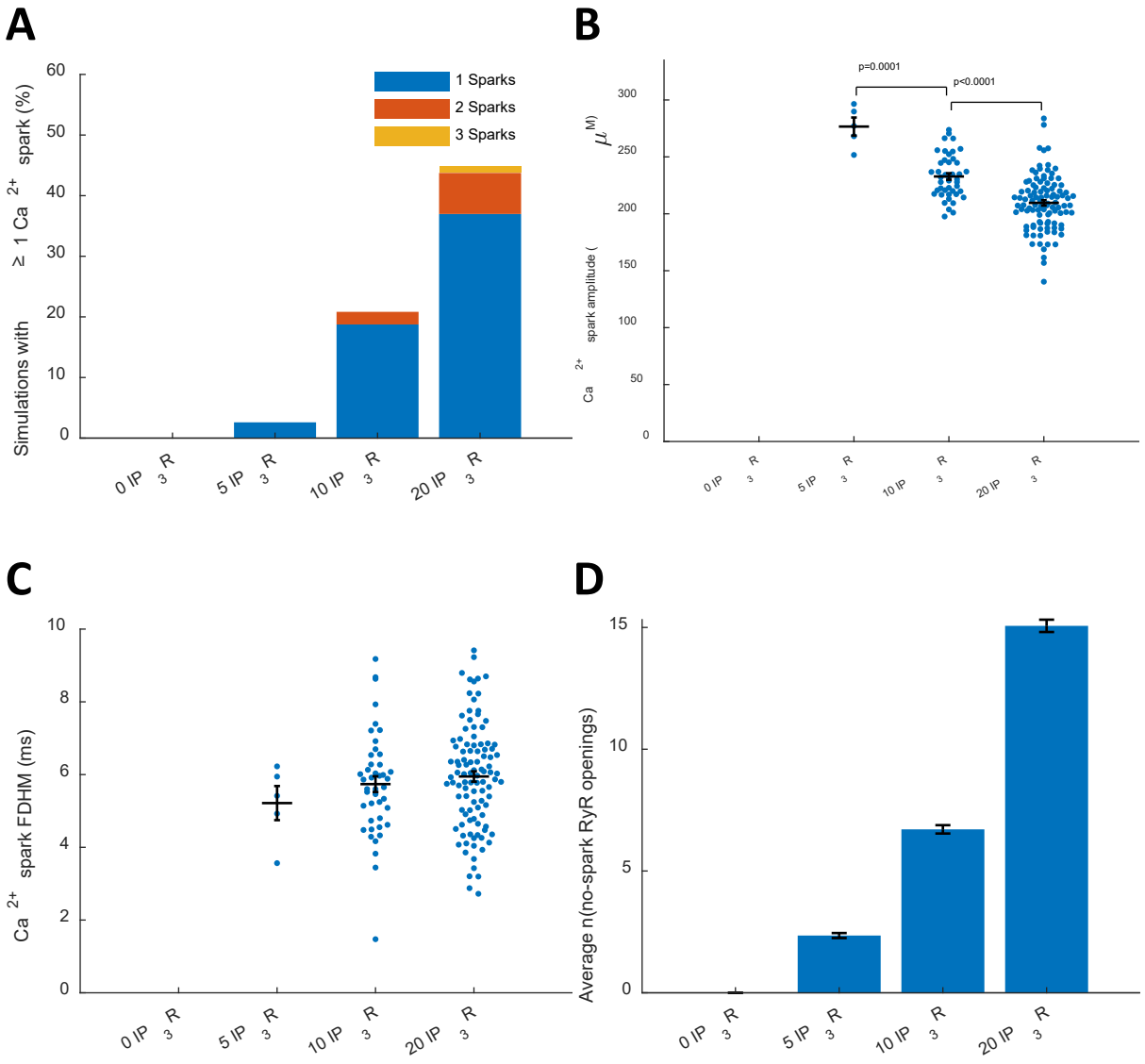

Figure 14. Simulations with randomly occurring Ca^{2+} "leak" fluxes from the JSR into the dyad qualitatively reproduced similar results as that with IP_3Rs. A: *Percentage of simulations where at least 1 spontaneous Ca^{2+} spark event occurred.* ***B:*** *Swarm plot showing the amplitude of spontaneous Ca^{2+} sparks that decreases with increasing equivalent number of IP_3Rs. Analysis by 1 way ANOVA with Tukey-Kramer post hoc test.* ***C:*** *Swarm plot showing the FDHM of spontaneous Ca^{2+} sparks that remains unchanged with the equivalent number of IP_3Rs. Analysis by 1 way ANOVA with Tukey-Kramer post hoc test.* ***D:*** *Average number of RyR opening events that do not lead to a Ca^{2+} spark increases with the equivalent number of IP_3Rs. All results presented in this figure were obtained from 200 simulations for each IP_3R number condition.*

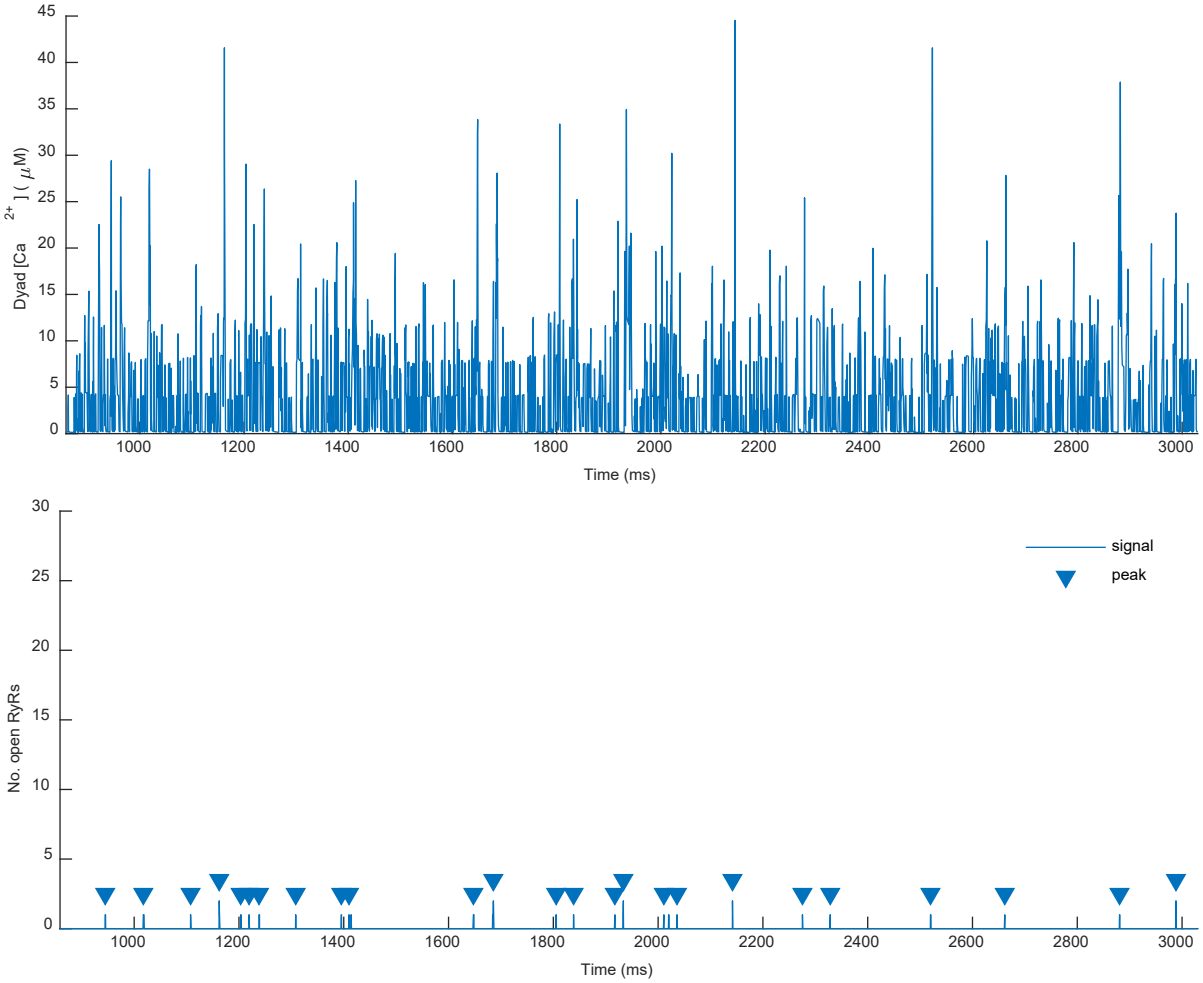

Figure 15. Dyadic [Ca²⁺] trace of a simulation that has no Ca²⁺ spark events. *Replacing IP_3Rs with a randomly occurring JSR Ca^{2+} leak flux leads to sporadic elevation of dyadic [Ca^{2+}] that reaches higher [Ca^{2+}] than that with a constant Ca^{2+} leak flux and is more successful at sensitizing RyRs.*

7.8 Model Robustness to Receptor Placement

The main results presented in this study were based on simulations of the model with RyRs and IP_3Rs placed at elements in the dyadic region as shown in **Figure 1**. To test the robustness of these results to changes in receptor placement, we ran similar simulations of the model whereby Ca^{2+} sparks are triggered. But this time the placement of RyRs and IP_3Rs in the dyadic region are randomly determined for each simulation. Results of these simulations are shown in **Figure 16** and are qualitatively similar to that shown in **Figure 3**. Therefore, the results obtained from our model is robust to changes in RyR and IP_3R placement.

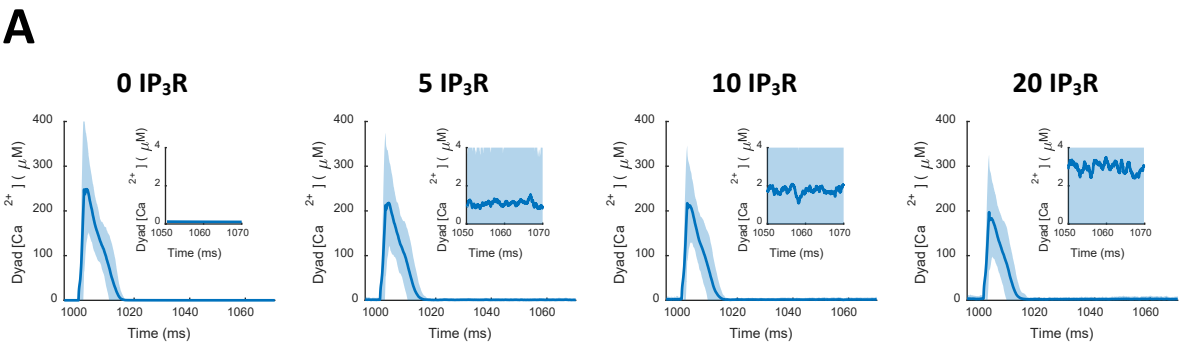

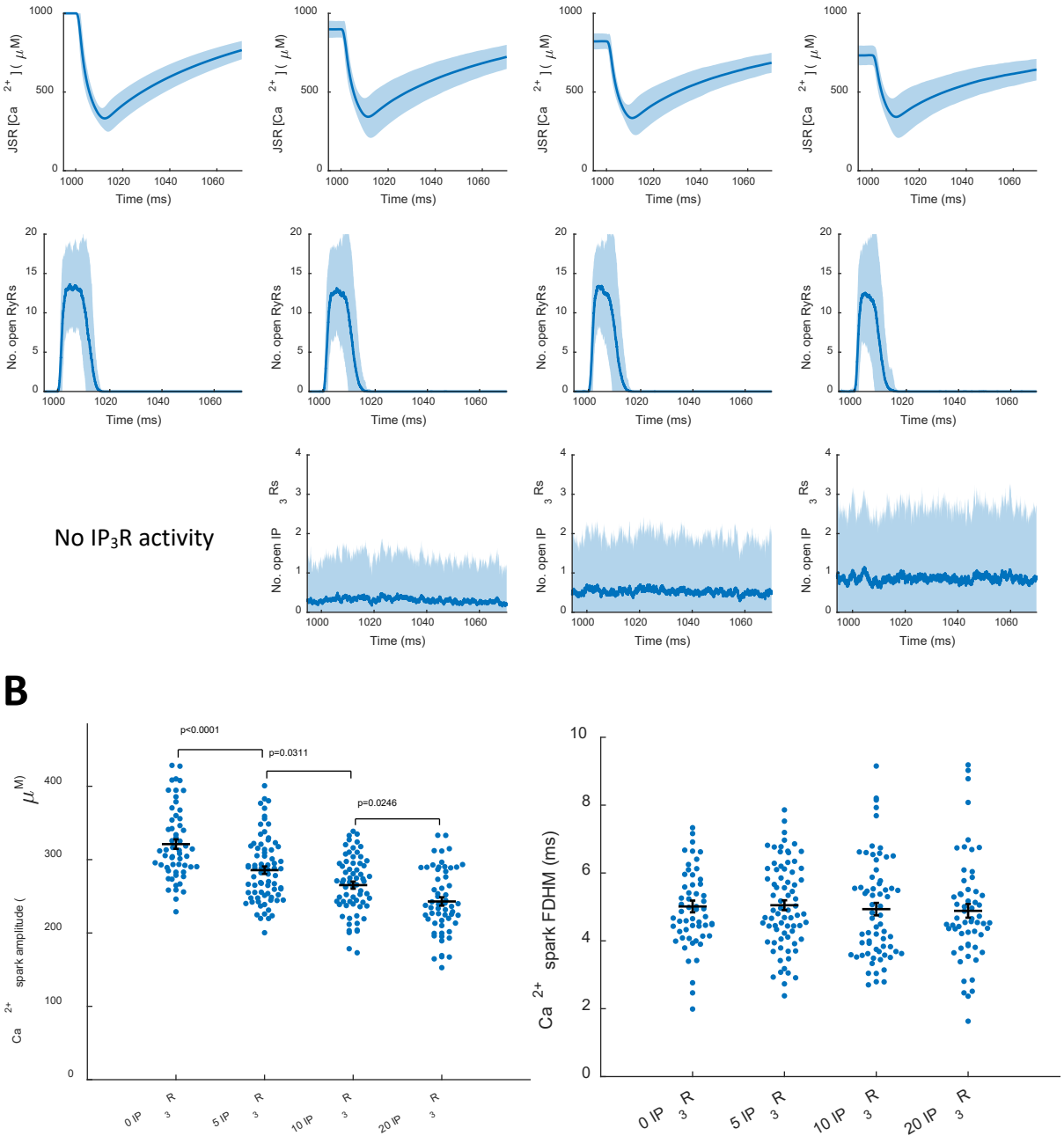

Figure 16. Ca^{2+} dynamics associated with LTCC-initiated Ca^{2+} sparks for simulations with randomly determined placement of RyRs and IP_3Rs. A: *From first to fourth row: Time evolution of dyadic [Ca^{2+}] (Insets show an average baseline dyadic [Ca^{2+}] that increases with the number of IP_3Rs), time evolution of JSR [Ca^{2+}], the number of open RyRs, and the number of open IP_3Rs associated with a Ca^{2+} spark. The mean and 95% confidence intervals, shown as solid lines and the surrounding shaded region respectively, are obtained from 200 simulations performed for each IP_3R number condition.* ***B:*** *Swarm plots showing a decreasing average Ca^{2+} spark amplitude but unchanged FDHM with increasing number of IP_3Rs. Analysis by 1 way ANOVA with Tukey-Kramer post hoc test. Data points were obtained from the same 200 simulations as that in* ***A****.*